

Testing Larson’s relationships in massive clumps

A. Traficante^{1*}, A. Duarte-Cabral², D. Elia¹, G. A. Fuller³, M. Merello¹, S. Molinari¹, N. Peretto², E. Schisano¹, and A. Di Giorgio¹

¹*IAPS - INAF, via Fosso del Cavaliere, 100, I-00133 Roma, Italy*

²*School of Physics and Astronomy, Cardiff University, Queens Buildings, The Parade, Cardiff CF24 3AA, UK*

³*Jodrell Bank Centre for Astrophysics, School of Physics and Astronomy, University of Manchester, Oxford Road, Manchester M13 9PL, UK*

9 March 2021

ABSTRACT

We tested the validity of the three Larson relations in a sample of 213 massive clumps selected from the Herschel Hi-GAL survey and combined with data from the MALT90 survey of 3mm emission lines. The clumps have been divided in 5 evolutionary stages to discuss the Larson relations also as function of evolution. We show that this ensemble does not follow the three Larson relations, regardless of clump evolutionary phase. A consequence of this breakdown is that the virial parameter α_{vir} dependence with mass (and radius) is only a function of the gravitational energy, independent of the kinetic energy of the system, and α_{vir} is not a good descriptor of clump dynamics. Our results suggest that clumps with clear signatures of infall motions are statistically indistinguishable from clumps with no such signatures. The observed non-thermal motions are not necessarily ascribed to turbulence acting to sustain the gravity, but they may be due to the gravitational collapse at the clump scales. This seems particularly true for the most massive ($M \geq 1000 M_{\odot}$) clumps in the sample, where also exceptionally high magnetic fields may not be enough to stabilize the collapse.

Key words: Stars – stars: formation – stars: kinematics and dynamics – stars: massive – stars: statistics – Resolved and unresolved sources as a function of wavelength – infrared: stars and Astronomical Data bases – surveys

1 INTRODUCTION

Massive star-forming regions are dominated by highly supersonic non-thermal motions. Velocity dispersions in giant molecular clouds (GMCs, size $\approx 5 - 100$ pc, Solomon et al. 1987), massive clumps (regions with size $\approx 0.5 - 2$ pc, e.g. Urquhart et al. 2014; Traficante et al. 2015a; Elia et al. 2017) and massive cores (size ≈ 0.1 pc, Zinnecker & Yorke 2007) are of the order of 1-10 km s⁻¹, significantly higher than thermal motions (≈ 0.25 km s⁻¹ for hydrogen molecules at typical temperature $T=15$ K).

The pioneering work of Larson (1981) investigated these motions in GMCs using the available ¹²CO data and found that the non-thermal motions may be ascribed to internal turbulence acting to sustain the clouds against the gravitational collapse. In this work Larson (1981) showed that molecular clouds follow three fundamental relations:

I : a size-linewidth power-law relation which states that in molecular clouds the velocity dispersion σ scales proportionally to the radius R . The first relation found by Larson was $\sigma \propto R^{0.38}$. Later the analysis was refined and the relation modified to $\sigma \propto R^{0.5}$ (e.g. Heyer & Brunt 2004).

II : clouds are in approximately virial equilibrium, with a virial

parameter $\alpha_{vir} = E_k/E_G = 5\sigma^2 R/GM \approx 1$, where M is the mass of the region and G the gravitational constant. This relation implies that the kinetic energy of the system $E_k \propto \sigma^2 M$ is of similar intensity as the gravitational energy of the system, $E_G \propto M^2/R$.

III : a volume density n -size relation, $n \propto R^{-1.1}$. This relation implies that GMCs are universal structures, with a mostly uniform column density. From this relation follows indeed that the surface density Σ is almost constant: $\Sigma \propto R^{-0.1}$.

Early observations of GMCs confirm the validity of the three relations (e.g. Solomon et al. 1987; Heyer & Brunt 2004), which were also observed in simulations of turbulent interstellar medium (Mac Low & Klessen 2004; McKee & Ostriker 2007, and references therein).

These relations were questioned however over the years. For example, the validity of the third relation was attributed to selection effects (e.g. Kegel 1989). The first and third Larson’s relations in GMCs were questioned by e.g. Heyer et al. (2009). This work re-analised the GMCs using ¹³CO data taken with the Boston University- FCRAO Galactic Ring Survey (GRS, Jackson et al. 2006). The higher critical density of ¹³CO compared to ¹²CO allowed to trace higher column density regions and these data demonstrate that the quantity $\sigma/R^{0.5}$ and the surface density of GMCs are not constant. Nevertheless, the average value of the virial param-

* e-mail: alessio.traficante@iaps.inaf.it

eter in GMCs, $\alpha_{vir}=1.9$, is still consistent with virial equilibrium (Heyer et al. 2009).

Challenging one of the Larson’s relation has direct consequences on the other two as well: the three relations are algebraically linked. If two of them are true, the third is automatically implied (e.g. Kritsuk, Lee & Norman 2013). At the same time, if one of the three is violated, necessarily (at least) one of the other two relations must not be true, with important implications on different star formation theories. The Larson’s relationships are in fact assumed in models that predict the formation of massive stars through turbulent-regulated collapse (e.g. McKee & Tan 2003), as opposed to gravity-dominated, almost free-fall collapse in which the theories predict for example values of the virial parameter $\alpha_{vir} < 1$ (e.g. Bonnell, Vine & Bate 2004).

While the validity of the Larson’s relations has been widely investigated in GMCs, few and relatively small surveys have been dedicated to the study of non-thermal motions in massive star forming clumps and cores. For example, Ballesteros-Paredes et al. (2011) showed that the first and third Larson’s relations are violated in GMCs and massive clumps. Simulations of star forming regions showed that ensemble of clouds, clumps and cores do not follow the three Larson’s relations, and this is particularly true for the higher density regions (Camacho et al. 2016). In a recent work we combined a survey of 16 massive $70\ \mu\text{m}$ quiet clumps with several surveys of massive dense cores at different evolutionary phases and showed that the three Larson’s relations seem to be violated in massive star-forming regions at the scales of clumps and cores (Traficante et al. 2018). However, a consistent analysis on a large sample of hundreds of massive star forming clumps at various evolutionary stages has not yet been performed.

In this work we examine the three Larson’s relations and their implications in a large sample of massive clumps obtained from the combination of the Elia et al. (2017) catalogue of clumps extracted from the *Herschel* Hi-GAL survey (Molinari et al. 2010), with the sample of molecular lines observed at 3mm with the MALT90 survey (Jackson et al. 2013). In Section 2 we describe the datasets used in this work and the selection of the final sample of 213 clumps with well defined dust and gas emission properties; in Section 3 we describe the classification scheme adopted for these clumps; in Section 4 we explore in detail the three Larson’s relations and we discuss the validity of these relations in massive clumps at different evolutionary stages; in Section 5 we analyze the implications of the previous results, in particular in the interpretation of the virial parameter; in Section 6 we study the properties of the clumps that show signs of infall motions and we compare these results with the rest of the sample; in Section 7 we explore possible explanations for the observed non-thermal motions; finally, in Section 8 we draw our conclusions.

2 DATASETS AND CLUMPS SELECTION

In the following we will describe the main datasets we have considered in this work, the selection criteria used to obtain the final sample and the estimation of the uncertainties on the main parameters used in the rest of the paper.

2.1 Hi-GAL data

The *Herschel* Hi-GAL survey observed the whole Galactic Plane in 5 wavelengths (70, 160, 250, 350 and $500\ \mu\text{m}$) using the two instruments, PACS (Poglitsch et al. 2010, 70 and $160\ \mu\text{m}$) and SPIRE

(Griffin et al. 2008, 250, 350 and $500\ \mu\text{m}$). This survey identified tens of thousands of filaments (Schisano et al. 2014) and point sources (Molinari et al. 2016b) across the Galaxy. The band-merged catalogue contains ≈ 100000 sources in the longitude range $-71^\circ \leq l \leq 67^\circ$ with defined spectral energy distributions and clump properties (Elia et al. 2017), from which we extracted the clumps used in this work.

2.1.1 Complementary dust continuum datasets

The Hi-GAL fluxes have been complemented at longer wavelengths with data at $870\ \mu\text{m}$ taken from the ATLASGAL survey (Schuller et al. 2009). This survey covers the Galactic longitudes $-80^\circ \leq l \leq 60^\circ$ with a spatial resolution of $19.2''$ and a sensitivity of $\approx 70\ \text{mJy/beam}$ (Csengeri et al. 2014). The ATLASGAL clumps catalogue (Csengeri et al. 2014) contains ≈ 10000 sources, including all the sources presented in this work.

The FIR-submm fluxes have been also complemented at shorter wavelengths with mid-infrared (MIR) data at $21\ \mu\text{m}$ (MSX, Egan, Price & Kraemer 2003), $22\ \mu\text{m}$ (WISE, Wright et al. 2010) and $24\ \mu\text{m}$ (MIPSGAL, Gutermuth & Heyer 2015). The MIR counterparts are described in the Elia et al. (2017) catalogue. We also used the results of the RMS survey (Lumsden et al. 2013) to classify the clumps. The RMS survey is a mid-infrared (MIR) selection of massive, evolved young stellar object (YSO) candidates across the whole Galaxy identified in MSX. Details of the survey can be found in Lumsden et al. (2013). The source counterparts at 21, 22 and $24\ \mu\text{m}$ have been used to determine the clumps evolutionary sequence according to the scheme proposed in Merello et al. (2018, in prep.) and summarized in Section 3.

2.2 MALT90 data

The MALT90 survey (Jackson et al. 2013) is a large survey of 90 GHz ($\approx 3\ \text{mm}$) emission lines associated with star forming regions. The survey observed 2012 clumps chosen from the ATLASGAL survey (Schuller et al. 2009). The clumps are distributed in the Galactic longitude ranges $3^\circ \leq l \leq 20^\circ$ in the first quadrant and $300^\circ \leq l \leq 357^\circ$ in the fourth quadrant. The survey has been carried out with the 22m Mopra telescope in on-the-fly mapping mode covering a region of $3.4' \times 3.4'$ across each clump, centred in the ATLASGAL clump centroid position. The FWHM is $38''$ at 90 GHz and the velocity resolution is $0.11\ \text{km s}^{-1}$. Typical system temperatures were in the range $180 \leq T_{sys} \leq 300\ \text{K}$, for a typical *r.m.s.* noise of $\approx 250\ \text{mK}$ per channel (Jackson et al. 2013). The MALT90 survey observed 16 different species spanning from dense gas tracers of relatively quiescent gas as the N_2H^+ ($1-0$), up to shock tracers as SiO ($1-0$) and ionised gas tracers as $\text{H41}\alpha$ (Jackson et al. 2013).

2.3 Clumps selection

We combined the datasets provided by the Hi-GAL and MALT90 surveys to identify a statistically significant sample of clumps with known distances and well defined dust and line emission properties.

From the 2012 Hi-GAL clumps also observed in the MALT90 survey we first excluded all clumps with longitudes $l \leq |10^\circ|$, for which the distance estimation may be highly inaccurate. We also excluded all the clumps with a mass estimation $M \leq 5 \times \sigma_{err}$, with σ_{err} the error associated with the mass estimation as discussed in Elia et al. (2017). We obtain a first selection of 617 clumps.

We further restricted our sample to well defined N_2H^+ (1 – 0) spectra that we used to estimate the gas velocity dispersion. The N_2H^+ (1 – 0) emission of each clump was evaluated from the MALT90 datacubes by averaging the spectrum across all the pixels within 1 MALT90 beam, $\approx 38''$. We assumed that all the N_2H^+ emission comes from the clumps, and we estimate the filling factor from the comparison of the radius of each Hi-GAL clumps with the radius of a region equal to the MALT90 beam (Figure 1). There is a strong correlation between these two quantities, and the size of the Hi-GAL clumps is systematically smaller than the radius estimated from the MALT90 beam for a factor of 0.64 on average. We assumed an average filling factor of 0.64 for the entire sample. The MALT90 datacubes are given in antenna temperature T_A^* and they have been converted in main beam temperature $T_{MB} = T_A^*/\eta_{MB}$, assuming a mean beam efficiency $\eta_{MB} = 0.49$ (Miettinen 2014). The properties of each N_2H^+ (1 – 0) averaged spectrum has been extracted in IDL using a hyperfine fitting routine and the `mpfitfun` algorithm (Markwardt 2009), after smoothing the data to a spectral resolution of 0.3 km s^{-1} to enhance the S/N ratio. We excluded all the clumps with a S/N below 5, where the *r.m.s.* in each smoothed datacube has been measured in a 100 km s^{-1} wide spectral window near the N_2H^+ emission. We further excluded clumps for which the fit converged but the spectrum was affected by spikes and/or by multiple components along the line of sight. Using this criteria, we obtained 308 clumps. We completed our selection excluding all clumps without a clear distance assignation, in particular without a well-defined resolution of the near-far distance ambiguity. First, we have refined the kinematic distances in the Elia et al. (2017) catalogue (and the quantities that depend on them) with the newest set of distances developed for the Hi-GAL survey under the VIALACTEA project (Mege et al. 2018, in prep.). The method used by Elia et al. (2017) was the same as in Russeil et al. (2011): the brightest emission line in the ^{12}CO or ^{13}CO spectra along the line of sight of each source are used to estimate the velocities of the local standard of rest and converted in heliocentric distances using the Brand & Blitz (1993) rotation curve. The Mege et al. (2018, in prep.) distances have been determined with a similar approach, but including all the recent surveys of the Galactic Plane to trace structures along the line of sight, and using the more recent Reid et al. (2009) rotation curve. Then, in order to identify only clumps with a well-defined distance estimation, we have compared the distances assigned to our 308 clumps with the distances of the MALT90 sample estimated in Whitaker et al. (2017) and of the ATLASGAL sources published in Urquhart et al. (2018). We excluded from the sample all the sources with a difference in the distance estimation larger than 20% among the three surveys.

We obtain a final selection of 213 clumps with well defined distances, dust properties and N_2H^+ spectra. The properties of these clumps are summarized in Appendix B.

2.4 Estimation of uncertainties

In this Section, we analyze the main source of uncertainties in both dust and gas properties of our 213 clumps. The results discussed in the next Sessions are significantly affected by the statistical uncertainties associated with each parameter, while they are not affected by uncertainties that produce systematic offsets.

The dust properties are mainly affected by the following source of uncertainties:

- Dust models for cold dust. The dust properties of the clumps in the Elia et al. (2017) catalogue have been evaluated assum-

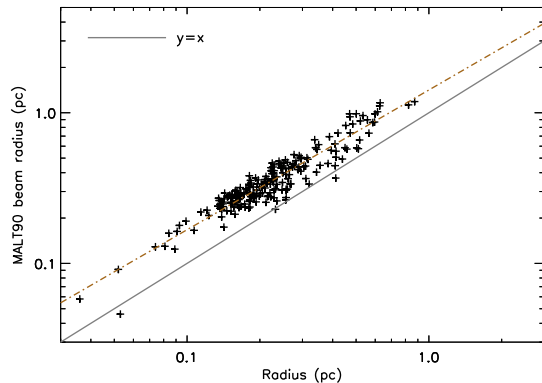


Figure 1. Comparison between radius of clumps as estimated at $250 \mu\text{m}$ and radius of a region equal to the size of a MALT90 beam. There is a strong correlation between the two values, and a systematic offset which shows that the MALT90 beam region is always bigger than the size of the Hi-GAL clump. The grey line is the $y=x$ line. The red-dashed line is the fit of the distribution. The offset between the two lines has been used to estimate the filling factor, which is 0.64.

ing a single-temperature greybody model with a spectral index $\beta = 2.0$, an opacity $\kappa_0 = 0.1$ at $\lambda_0 = 300 \mu\text{m}$ (Beckwith et al. 1990), and a gas-to-dust ratio of 100. The commonly used model of Ossenkopf & Henning (1994), assuming a thin ice mantle and a gas density of 10^6 g cm^{-3} leads to $\kappa_0 = 0.17$ at $\lambda_0 = 300 \mu\text{m}$, a difference of almost a factor of 2 from the Beckwith et al. (1990) opacity. Since the mass estimate scales linearly with the opacity, using a different model would lead to a systematic offset in the mass, surface density (positive offset for higher values of κ_0) and virial parameter estimates (negative offset). Our results are however not affected by systematic offsets. The spectral index β can vary across different sources as function of the dust temperature (Paradis et al. 2010), as well as function of the dust column density (Juvela et al. 2015). With a variation of the spectral index $\beta = 2.0 \pm 0.3$ (in line with the findings of Paradis et al. 2010), the mass change for a factor of $\approx 30\%$. We consider this value as the uncertainties on the mass estimation due to the assumed dust model.

- Errors in distance estimation. These uncertainties are due to: 1) the method used to estimate the radial velocities. The distances presented in the Mege et al. (2018, in prep.) catalogue are evaluated with a method similar to the one adopted in Urquhart et al. (2018). In this work the authors calculated an uncertainties on the distance estimation of $\approx 0.30 \text{ kpc}$. Our final sample of 213 sources is at a mean distance of $\approx 4.2 \text{ kpc}$, which gives an error of $\approx 7\%$ on the distance estimation due to the adopted method; 2) the rotation curve adopted to convert the radial velocities into kinematic distances. The work of Russeil et al. (2011) compared the distance obtained using the Brand & Blitz (1993) and the Reid et al. (2009) rotation curves and showed that, within the uncertainties, the results are compatible. Therefore, the results are not greatly affected by different rotation curves; 3) the near-far distance ambiguity. As discussed in Section 2.3, we have selected only the conservative, but most reliable sub-sample of sources with the same solution for the near-far distance ambiguity in the Hi-GAL (Mege et al. 2018, in prep.), ATLASGAL (Urquhart et al. 2018) and MALT90 (Whitaker et al. 2017) catalogues. We therefore assumed that the distance ambiguity has been solved for our sub-sample of sources. These sources have a distance determination that differs up to

20% with respect to the values in the ATLASGAL and MALT90 catalogues, but on average the difference is of only 4%. Combining these results, we conservatively assume that the distance uncertainties are of the order of 15%. The same uncertainties are associated with the radius R . The mass depends on distance as $M \propto d^2$, so the mass uncertainties due to the distance uncertainties are $\approx 30\%$.

- **Uncertainties on radius estimation.** The angular radius of each clump is defined as the geometrical mean R_{eq} of the 2 FWHMs of the Gaussian fit done at $250 \mu\text{m}$ (Elia et al. 2017). The majority of these sources are however elongated along one direction, and this asymmetry produces uncertainties in the definition of the source radius. We estimated these uncertainties by taking the differences between R_{eq} and the minor and major axis of each source. The average differences are of the order of 10% of the geometrical mean, with peaks up to 50% and a standard deviation of $\approx 10\%$. We consider a conservative value of 20% on the uncertainties associated with the radius estimation due to the geometrical mean approximation.

- **Results of the SED fitting routine.** Mass and temperature are estimated only for clumps that have at least three consecutive fluxes in the Hi-GAL wavelengths $160 \leq \lambda \leq 500 \mu\text{m}$, and irregular SEDs are not considered (Elia et al. 2017). The clumps in our sample have well defined properties and the uncertainties associated with the fitting routine are very small. They are of the order of 1.5%, with a peak of 18%. We assume an average error of 5% associated with the SED fitting.

- **Choice of the photometry algorithm.** In Appendix A we discuss how the estimates of properties such as the mass differ from the values of the Elia et al. (2017) catalogue using a different algorithm to evaluate the source photometry (*Hyper*, Traficante et al. 2015b). The differences in the estimation of the fluxes produce a systematic offset of 10% in the mass values, which do not bias the results of this work. The statistical uncertainties are of the order of $\approx 25\%$, that we assume as the uncertainties on the mass estimation due to the photometry method. In Appendix A we also show that our results are robust against these differences, and they are not biased by the specific algorithm used to extract the properties of the clumps.

The uncertainties associated with the estimation of the non-thermal velocity dispersion are dominated by the spectral resolution of our observations. The hyperfine fitting has been done on spectra smoothed three times, and the uncertainties on the fit are of the order of the smoothed spectral resolution, 0.3 km s^{-1} . The average non-thermal component of the velocity dispersion is $\approx 1.21 \text{ km s}^{-1}$, so the error derived from the hyperfine fit is of the order of the 25% of the measured non-thermal velocity dispersion.

The intensity of the thermal component to be subtracted from the observed velocity dispersion could be another source of uncertainties. We estimated this component assuming for the gas the same temperature of the clump, which span a range $8.5 \leq T \leq 40 \text{ K}$. The N_2H^+ thermal component within this range of temperatures is much smaller than the non-thermal component, and varies in the range $0.05 \leq \sigma_{th} \leq 0.11 \text{ km s}^{-1}$. Even accounting for a gas temperature which differs substantially from the estimated dust temperature, the error is $\sigma_{th,unc} \lesssim 0.05 \text{ km s}^{-1}$. This is smaller than 5% of the measured velocity dispersion. We assume a conservative error of 5% from the subtraction of the thermal component to the estimation of the non-thermal motions.

The uncertainties on the main parameters used in this work are summarized in Table 1. The uncertainties on α_{vir} has been evaluated using the standard formula for the propagation of uncertainties.

3 CLUMPS CLASSIFICATION SCHEME

The association between our 213 Hi-GAL clumps and counterparts in the MIPS GAL, WISE and RMS surveys are used to determine an evolutionary sequence for our sources. The association with MIPS-GAL and WISE has been taken from the Elia et al. (2017) catalogue. The association with RMS has been done looking for RMS counterparts of the Hi-GAL sample within a radius equal to the geometrical mean of the FWHMs of each source.

We adopted the evolutionary scenario based on the Hi-GAL survey and presented in Merello et al. (2018, in prep.). These authors analyzed ≈ 1000 Hi-GAL clumps and followed a similar approach to the one used by König et al. (2017), but divided the clumps in 5 different evolutionary phases: 1) a starless phase, identified as bright regions at wavelengths $\lambda \geq 160 \mu\text{m}$ but still dark at wavelengths $\lambda < 100 \mu\text{m}$; 2) protostar MIR dark, when a clump becomes visible at $70 \mu\text{m}$ but it is still dark in the MIR, or the emission too faint to be identified. These clumps are bright at all Hi-GAL wavelengths, with no counterparts in the MIPS GAL, WISE and RMS surveys; 3) protostar MIR bright, when the clumps become visible also in the MIR and their bolometric luminosity increases significantly. These clumps have at least a counterpart in one among MIPS GAL, WISE and MSX surveys but they do not pass the RMS criteria to be classified as YSOs (Lumsden et al. 2013); 4) YSOs, when the protostars have reached the zero-age main sequence and become bright also in the NIR regime. They are classified as YSOs in the RMS survey; 5) HII regions, where the thermal bremsstrahlung emission of the gas ionized in the envelope of the more massive stars can be observed at radio wavelengths (Wood & Churchwell 1989). Radio observations are used to identify HII regions among YSOs (Hoare et al. 2007). These sources have been classified as either UCHII or extended HII regions in the RMS catalogue. The classification scheme is summarized in Table 2.

Based on this classification scheme, we have identified: 14 starless, 12 protostars MIR dark, 106 protostars MIR bright, 25 YSOs and 56 HII regions, among which 14 are extended HII regions. This classification is consistent with the results we obtain from a well-known indicator of clumps evolution, the luminosity over mass (L/M) ratio (Molinari et al. 2008; Molinari et al. 2016a). As showed in Figure 2, the L/M ratio of these clumps spans more than four order of magnitudes in total, and increases from starless to HII regions. In agreement with the findings of Merello et al. (2018, in prep.), there is no significant differences in L/M between MIR dark and MIR bright sources, suggesting that the presence of a MIR source in a clump do not alter significantly the total luminosity of the cold dust envelope.

In Figure 3 we present the Galactic distribution of our sources, overlaid with the four spiral-arms Galactic model of Hou, Han & Shi (2009). All sources are located in the IV Quadrant. They are mostly concentrated in a region between the Crux-Scutum and the Norma arms, and the inter-arms region.

In the next Sections we will investigate the gravo-turbulent properties of these clumps, in light of this classification scheme.

4 LARSON'S RELATIONS IN MASSIVE CLUMPS

In this Section we analyse the three Larson's relations in our clumps and we discuss the implications of the results.

Parameter	Relative uncertainties (%)	Source of uncertainties
R	25	distance, geometrical mean
M	50	β index, distance, SED fitting, photometry method
Σ	35 ¹	β index, SED fitting, photometry method
σ	30	hyperfine fitting, thermal motions
α_{vir}	65	M, R, σ

¹ The uncertainties on Σ depend only on the SED fitting and are independent of the source distance.

Table 1. Relative uncertainties associated with the main parameters used in this work. Col. 1: Parameters; Col. 2: relative uncertainties, as estimated from the discussion in Section 2.4; Col. 3: sources of uncertainties used to estimate the relative uncertainties on the parameters.

Evolutionary phase	Bright wavelengths (μm)	Survey	L/M (L_{\odot}/M_{\odot})	Count
Starless	>70	Hi-GAL	1.7	14
Protostellar MIR dark	≥ 70	Hi-GAL	8.4	12
Protostellar MIR bright	≥ 21	Hi-GAL, MIPS GAL, WISE	6.4	106
YSOs	≥ 8	Hi-GAL, MIPS GAL, WISE, RMS	32.1	25
HII regions (UCHII + ext. HII)	≥ 8 & radio emiss.	Hi-GAL, MIPS GAL, WISE, RMS	36.3	56 (42+14)

Table 2. Classification scheme of our 213 clumps following the evolutionary scenario described in Merello et al. (2018, in prep.). Col 1: Evolutionary phase; Col. 2: wavelengths at which each evolutionary stage becomes bright; Col. 3: Survey with a visible counterpart in the data; Col.4: median value of L/M; Col. 5: Number of identified objects.

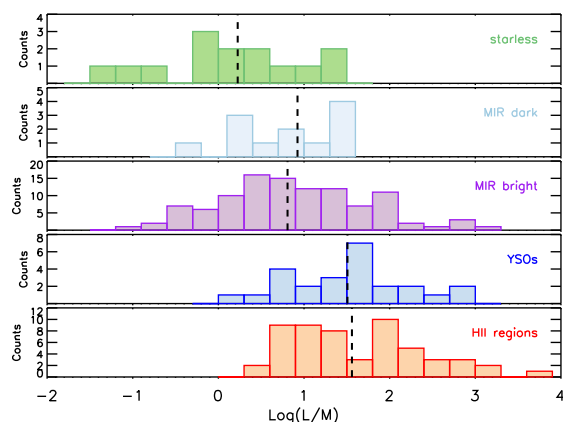


Figure 2. L/M ratio distribution of our 213 clumps divided for the various evolutionary phases. The entire sample spans more than 4 order of magnitudes and there is an evident increase of the L/M ratio going from starless to HII regions.

4.1 Larson's first relation: linewidth-size

The Larson's first relation shows the proportionality between the size of GMCs and the non-thermal motions of the gas in the region (Larson 1981). This relation has been often considered to be due to the interstellar turbulence. The interstellar medium modeled as a turbulent fluid dominated by shocks follows a power-spectrum relation of the form $R \propto \sigma^{0.5}$ (i.e. a Burgers-like power-spectrum $E_k \propto k^{-2}$, e.g. McKee & Ostriker 2007), a scenario that reproduces the large-scale observations (Padoan & Nordlund 2002; McKee & Ostriker 2007). However, the relation seems to break in massive clumps embedded in molecular clouds. For example, Caselli & Myers (1995) observed the Orion A and B high-mass star forming regions and found a correlation between size and velocity dispersion of the form $R \propto \sigma^{0.21}$, significantly lower than that

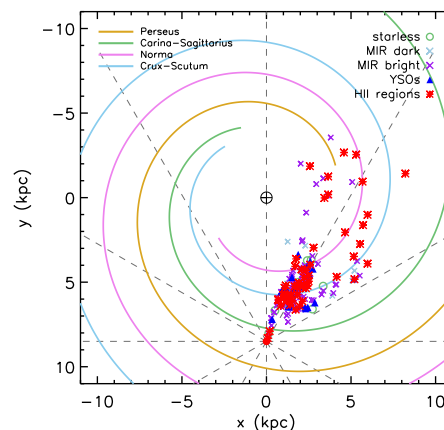


Figure 3. Galactic distribution of the 213 clumps investigated in this work. Colours and symbols represent clumps at different evolutionary stages. Overlaid is the Galactic model of Hou, Han & Shi (2009), the same used to discuss the clumps distribution in Elia et al. (2017). All clumps are in the IV Quadrant, mostly distributed across the Crux-Scutum and Norma arms and in the inter-arms region. The red-filled dot at [0.8, 5] kpc represents the position of the Sun. The black circle at [0, 0] kpc is the Galactic Center.

found in GMCs. Similar results have been obtained in the survey of high-mass star forming regions of Shirley et al. (2003). At the same time, other surveys of massive star-forming objects found no correlation (Plume et al. 1997; Ballesteros-Paredes et al. 2011; Traficante et al. 2018) or even an inverse correlation (Wu et al. 2010) between size and linewidth.

In Figure 4 we report the velocity dispersion-radius relationship for our sample of 213 sources. The slope of the linear fit in the log-log space is 0.09 ± 0.04 , suggesting that a correlation between velocity dispersion and radius, if present, is very low. The fit in this plot (and for the rest of this work) has been obtained from a linear regression done with the `fitexy` IDL routine, which per-

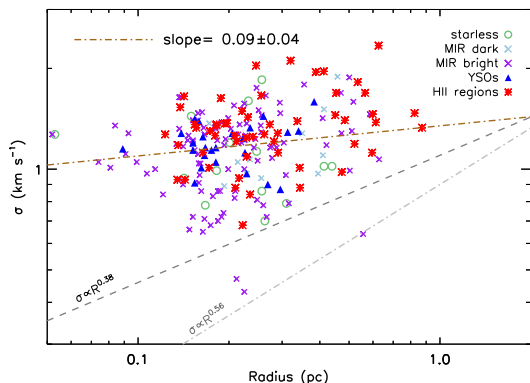


Figure 4. First Larson relation: velocity dispersion σ as function of the radius R . The dark grey dashed line is the original Larson’s relation, $\sigma \propto R^{0.38}$, the light grey dash-dotted line is the revised Heyer & Brunt (2004) relation, $\sigma \propto R^{0.56}$. The correlation is weak, with a Pearson’s coefficient of $\rho = 0.26$.

forms a chi-square approximation when uncertainties are known in both the x and y variables. The Pearson’s correlation coefficient ρ , which measures the linear correlation between two variables and varies in the range $-1 \leq \rho \leq 1$, with $\rho = -1$ indicating total anti-correlation, $\rho = 1$ total correlation and $\rho = 0$ no correlation, has a value $\rho \approx 0.26$, also suggesting that a correlation between these two variables is rather weak.

In Figure 5 we report the quantity $\sigma/R^{0.5}$ divided for the different evolutionary stages. Following the first Larson’s relation, this quantity should be a constant of the system. Instead, we find a distribution of this quantity across a range $0.9 \leq \sigma/R^{0.5} \leq 12.8$ $\text{km s}^{-1} \text{pc}^{-0.5}$, larger than the estimate uncertainties of size and velocity dispersion combined (see Section 2.4). Also, within uncertainties there is no distinction between different evolutionary phases, with median values of $[2.32, 2.21, 2.66, 2.73, 2.60]$ $\text{km s}^{-1} \text{pc}^{-0.5}$ in the starless, protostar MIR dark, protostar MIR bright, YSOs and HII regions phases respectively. Altogether or divided for different evolutionary phases, these results suggest that the first Larson’s relation typically breaks down at clump scales, and this break is not due to the different internal conditions of these objects.

The observed first Larson’s relation implies that one, or both of the other two relations must not be followed by this ensemble of clumps.

4.2 Larson’s second relation: the virial equilibrium

The second Larson’s relation states that GMCs are approximately in virial equilibrium. The virial parameter α_{vir} has been often interpreted as representative of the equilibrium between E_k and E_G when all other forces such as magnetic fields are not involved (and assuming spherical and homogeneous density distribution, Bertoldi & McKee 1992). The virial equilibrium implies $\alpha_{vir} = \alpha_{eq} = 1$ or, if a collapsing cloud is modeled as an isothermal (Bonnor-Ebert) sphere, the hydrostatic equilibrium is at $\alpha_{eq} \approx 2$ (Kauffmann, Pillai & Goldsmith 2013; Tan et al. 2014). GMCs are expected to be in virial equilibrium, with the kinetic energy due to local turbulence that provides support against the gravitational collapse (McKee & Tan 2003; Heyer et al. 2009). The formation of massive clumps in a gravo-turbulent collapse is also predicted to

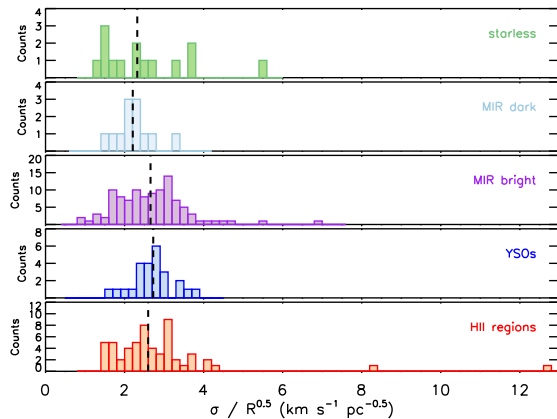


Figure 5. First Larson’s relation distribution for our clumps, divided for different evolutionary stages. The relation states that the quantity $\sigma/R^{0.5}$ should be a constant. Instead, the distributions span a range of values for each evolutionary phase.

Evolutionary phase	α_{vir}
Starless	$0.07 \leq \alpha_{vir} \leq 7.98$
MIR dark	$0.13 \leq \alpha_{vir} \leq 1.71$
MIR bright	$0.07 \leq \alpha_{vir} \leq 3.52$
YSOs	$0.20 \leq \alpha_{vir} \leq 2.03$
HII regions	$0.05 \leq \alpha_{vir} \leq 12.81$

Table 3. Range of values of α_{vir} in our clumps for each stage of evolution. Col. 1: Evolutionary phase; Col. 2: Range of values of α_{vir} .

happen in a state of global virial equilibrium (Lee & Hennebelle 2016).

Alternatively, the observed non-thermal motions may partly be the result of the collapse itself, and not necessarily providing support against gravity. In this interpretation virial equilibrium loses its original meaning. The regions would be in approximately virial equipartition (which also implies $\alpha_{eq} = 2$), but misinterpreted as in virial equilibrium (Ballesteros-Paredes 2006).

Independently of the interpretation of the observed α_{vir} , there is a general consensus that regions with $\alpha_{vir} < \alpha_{eq}$ are gravitationally bound and prone to collapse, if not sustained by strong magnetic fields which may stabilize them (e.g. Kauffmann, Pillai & Goldsmith 2013). These regions do not follow the second Larson’s relation.

Figure 6 shows the distribution of the virial parameter of our 213 clumps divided in the five evolutionary stages, and in Table 3 we report the range of α_{vir} for each phase. The virial parameter spans the range $0.05 \leq \alpha_{vir} \leq 12.8$, and each evolutionary phase spans at least one order of magnitude, with no clear differences between the various stages of evolution. A total of 51 clumps have $\alpha_{vir} \geq 1$, and only 14 have $\alpha_{vir} \geq 2$. The majority of our clumps are gravitationally bound and these clumps, if not sustained by strong magnetic fields (see Section 7.3), are not in gravitational equilibrium. If the kinetic energy is due to turbulence acting to support gravity, its contribution is not sufficient to stop or slow-down the collapse at the clump scales.

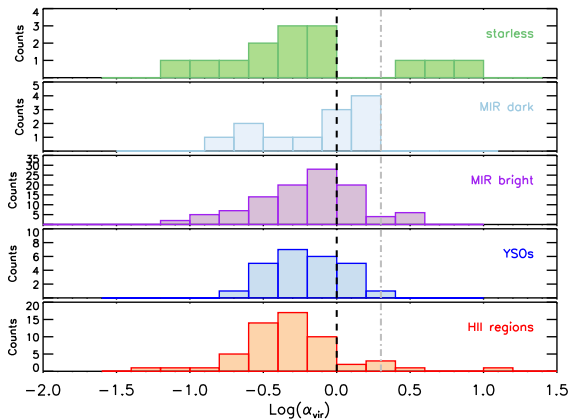


Figure 6. Histogram of the α_{vir} distribution at different evolutionary stages. The majority of the clumps have $\alpha_{vir} \leq 2$, independently from the evolutionary phase. The black dashed line is in correspondence of $\alpha_{vir}=1$, and the grey dash-dotted line is at $\alpha_{vir}=2$.

4.3 Larson's third relation: mass-radius diagram

A practical form of the Larson's third relation states that molecular clouds have approximately the same surface density: $\Sigma \propto nR \propto R^{-0.1}$. This formulation is much easier to verify experimentally, since it does not require placing any constraints on the third dimension needed to evaluate the volume density of the observed regions.

The early observations of Larson (1981) suggest that GMCs have all similar column densities. However, the third Larson's relation may simply be an observational bias due to the molecular tracer used in early GMC observations (e.g. Kegel 1989; Ballesteros-Paredes 2006; Heyer et al. 2009). Using extinction as a tracer of molecular gas, Lombardi, Alves & Lada (2010) demonstrated that the third Larson's relation is observed in nearby molecular clouds only above a given surface density threshold. The relation does not hold in clumps and cores embedded in single clouds, and an apparent density-size relation may be observed as an artifact of clumps limited within column density thresholds (Camacho et al. 2016). Indeed, several surveys of massive clumps have shown that they span almost two order of magnitude in surface densities (Urquhart et al. 2014; Traficante et al. 2015a; Svoboda et al. 2016; Elia et al. 2017).

The surface densities of the 213 clumps analysed in this work are in Figure 7. The surface densities are in the range $0.13 \leq \Sigma \leq 8.57 \text{ g cm}^{-2}$, spanning more than one order of magnitude in each evolutionary phase. We found median values of [0.83, 0.45, 0.80, 0.98, 0.99] g cm^{-2} in starless, protostar $24 \mu\text{m}$ dark, protostar $24 \mu\text{m}$ bright, YSOs and HII regions respectively. Within the uncertainties in the estimation of the surface densities (35% of their value, Table 1), the median distribution are likely indistinguishable, in agreement with with the findings of Urquhart et al. (2014) and Svoboda et al. (2016), and with the results presented in Merello et al. (2018, in prep.). The surface density of each clump may be more likely related with the density properties of the local environment, regardless of its evolution.

4.3.1 Mass-radius relationship

An alternative way to look at the third Larson's relation is through the mass-radius diagram. A sample of star-forming regions with roughly constant column density should have a mass distribu-

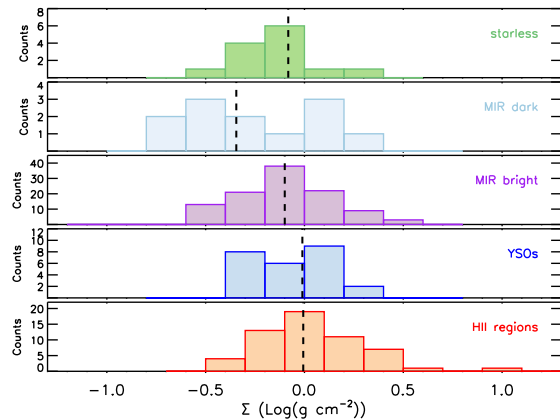


Figure 7. Surface density distribution of the clumps separated for each evolutionary phase. The black vertical lines are in correspondence of the median values of Σ in each evolutionary stage. The surface density values span more than one order of magnitude, and there is no clear evidence of a trend with evolution.

tion $M \propto R^\delta$ with $\delta \approx 2$. Previous surveys of massive clumps have found a large range of values for δ , which is strongly dependent of the different strategies used to extract the dust properties of the clumps. Mass-radius diagrams have been observed with slopes in the range $\delta \approx 1.6 - 1.7$ (Lombardi, Alves & Lada 2010; Kauffmann et al. 2010; Urquhart et al. 2014), as well as with $\delta \geq 2$ (Ellsworth-Bowers et al. 2015) or even greater ($\delta \geq 2.7$, Ragan, Bergin & Gutermuth 2009).

In Figure 8 we show the mass-radius diagram of our clumps. The fit has a slope $\delta = 2.38 \pm 0.10$, not in agreement with constant Σ . We investigated how much this result is sensitive to the estimated uncertainties by modifying the errors associated with the parameters of $\pm 10\%$. We obtained a difference of up to 5% in the value of the slope, which varies in the range $2.19 \pm 0.09 \leq \delta \leq 2.53 \pm 0.13$. Also accounting for these variations, the slope is not consistent with constant surface density, as expected from the large spread showed in Figure 7.

The mass-radius diagram is also a useful tool to investigate clumps which may likely form high-mass stars. The vast majority of these clumps may form high-mass objects, following the empirical mass-radius thresholds determined by Kauffmann & Pillai (2010) and Baldeschi et al. (2017). All but two clumps (G333.449-00.183 and G338.917+00.382) are above the former, and all but three clumps (G333.449-00.183, G338.917+00.382 and G343.938+00.097) are above the latter, which is a more stringent threshold.

To conclude this Section, we have shown that the Larson's relations do not describe the dynamical properties of an ensemble of (massive) clumps. In the next Section we will explore some implications of this evidence.

5 VIRIAL PARAMETER DEPENDENCES

A consequence of the breakdown of the Larson's relations in massive clumps is the dependence of the virial parameter with the dust properties of these regions (mass and radius). There is an observed trend of decreasing virial parameter at increasing mass, which is interpreted as the most massive regions are also the more gravitationally bound. For example, the massive star-forming regions analyzed by Urquhart et al. (2014) showed a power-law form $\alpha_{vir} \propto M^\alpha$

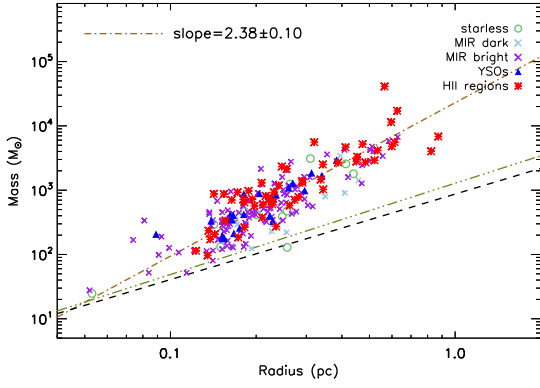


Figure 8. Mass versus radius distribution. The green dash-dotted line is the Kauffmann & Pillai (2010) massive star formation threshold ($M(r) > 870 M_{\odot} (R/\text{pc})^{1.33}$), and the black dashed line is the revised Baldeschi et al. (2017) threshold ($M(r) > 1282 M_{\odot} (R/\text{pc})^{1.42}$). The red dashed line is the best fit to our sample, $M \propto R^{2.38 \pm 0.10}$.

with $\alpha = -0.53 \pm 0.16$. Similarly, Kauffmann, Pillai & Goldsmith (2013) found a slope varying in the range $-1 \leq \alpha \leq -0.4$ among various surveys of massive clumps and cores.

As noted by Kauffmann, Pillai & Goldsmith (2013), the slope α depends also on both the first and third Larson’s relationships:

$$\frac{d \log(\alpha)}{d \log(M)} = \frac{2 \frac{d \log(\sigma)}{d \log(R)} + 1 - \frac{d \log(M)}{d \log(R)}}{\frac{d \log(M)}{d \log(R)}} \quad (1)$$

If the size and velocity dispersion in star forming regions are not correlated, $d \log(\sigma)/d \log(R) = 0$. Equation 1 becomes:

$$\frac{d \log(\alpha)}{d \log(M)} = \frac{1 - \frac{d \log(M)}{d \log(R)}}{\frac{d \log(M)}{d \log(R)}} \quad (2)$$

which implies that the slope of the α_{vir} -mass diagram depends *only* on the slope of the mass-radius diagram.

Applying Equation 2 to our clumps, since the mass-radius slope is $\delta = 2.38 \pm 0.10$ (see Section 4.3), the predicted α_{vir} -mass slope is $\alpha = -0.58 \pm 0.02$. In Figure 9 we show the α_{vir} vs. mass diagram. We found a slope $\alpha = -0.56 \pm 0.04$, in agreement with the prediction of Equation 2. The fit is robust against the estimation of the uncertainties, with a variation of less than $\approx 1\%$ assuming a variation of $\pm 10\%$ on the errors associated with M and α_{vir} .

Similarly, the slope of the virial parameter-radius diagram is

$$\frac{d \log(\alpha)}{d \log(R)} = 2 \frac{d \log(\sigma)}{d \log(R)} + 1 - \frac{d \log(M)}{d \log(R)} \quad (3)$$

In the case where the first Larson’s relation is not valid, the slope depends, again, only on the slope of the mass-radius diagram.

The slope of the α_{vir} -radius diagram predicted from Equation 3 is $\alpha_r = -1.38 \pm 0.06$. The α_{vir} -radius diagram is in Figure 10 and the slope is $\alpha_r = -1.13 \pm 0.10$, slightly lower than the predicted value. This fit is also the most sensitive to the estimation of the uncertainties. A variation of $\pm 10\%$ on the errors associated with R and α_{vir} leads to a difference of more than 50% in α_r , which varies in the range $-0.97 \pm 0.10 \leq \alpha_r \leq -1.50 \pm 0.12$, within the prediction of Equation 3.

These results show that in our sample the kinematic properties of the clumps do not affect the distribution of the virial parameter, which are driven by the dust properties (mass and size) of these

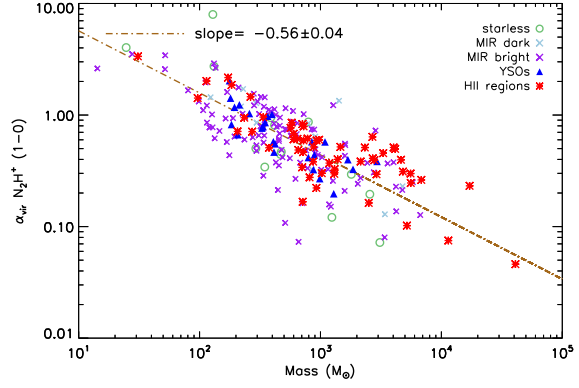


Figure 9. Virial parameter distribution as function of mass. The red dashed line is the best-fit to our data, which gives a slope $\alpha = -0.56 \pm 0.04$.

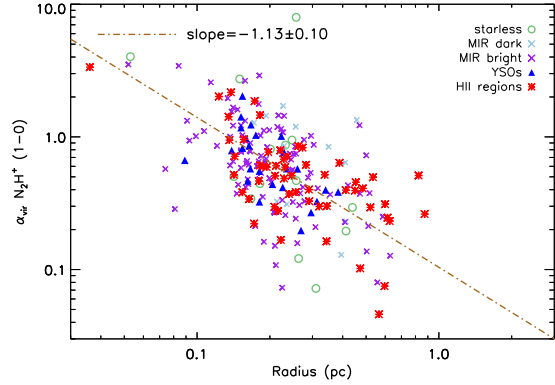


Figure 10. Distribution of the virial parameter as function of clumps radius R . The best-fit line has a slope of $\alpha_r = -1.13 \pm 0.10$.

sources. In other words, the concept of virial equilibrium may be misleading: in a sample that violates the three Larson’s relations the virial parameter varies independently from the kinetic energy of the sources.

Note that these results are valid for an ensemble of clumps, where the non-thermal motions are estimated with a single gas tracer. This common choice however biases the observations toward regions with similar volume densities within each clump, regardless of the clumps physical properties (i.e. of mass and size). The correlation between α_{vir} and mass seems indeed to disappear when different surveys of clumps and cores observed with different tracers are combined together (Kauffmann, Pillai & Goldsmith 2013). These results may differ from the analysis of the energy balance within single star-forming regions. They may all be near virial equilibrium, as predicted by e.g. Lee & Hennebelle (2016), but the kinetic energy in the more massive clumps could not be properly measured.

The virial parameter determined for an ensemble of massive clumps may not be a good descriptor of the clumps dynamics, an hypothesis that we will explore in the next Section.

6 INFALLING PROPERTIES

If the virial parameter is not a good descriptor of the energy balance in an ensemble of massive clumps, these regions may be gravitationally bound and collapsing independently from the value of α_{vir} . One way to explore this hypothesis is to compare the properties of clumps with signs of infall motions against clumps with no such signatures.

The MALT90 survey observed also the $\text{HCO}^+ (1-0)$ transition, an optically thick line and a good tracer of infall motions (Fuller, Williams & Sridharan 2005; Rygl et al. 2013; He et al. 2015; Traficante et al. 2017). These motions can be identified looking at blue asymmetries in the spectra in correspondence of single-peaked $\text{N}_2\text{H}^+ (1-0)$ spectra, which avoid the risk that the asymmetries in the $\text{HCO}^+ (1-0)$ spectra may be due to the obscuration by surrounding filaments (Chira et al. 2014).

We identified by eye all clumps with well defined infall signatures, i.e. all clumps with double-peaked blue-asymmetric $\text{HCO}^+ (1-0)$ spectra, and we found 21 clumps with such properties. This number likely represents a sub-sample of clumps that have parsec-scale infall motions. Many clumps may present red-asymmetric $\text{HCO}^+ (1-0)$ spectra despite the presence of infall motions that can be identified with blue-asymmetric spectra in higher density tracers (Wyrowski et al. 2016). Also, infalling clumps may not always show the expected blue-asymmetric line profiles (Smith et al. 2013). At the same time, well-defined blue-asymmetries in the $\text{HCO}^+ (1-0)$ spectra are clear signatures of infall motions and can be modeled to infer infall parameters (see next Section), therefore we restrict the analysis to this sub-sample of 21 clumps to analyze the main infall properties of our sample. These clumps are divided in 10 protostar MIR bright, 4 YSOs, and 7 HII regions.

The clumps with infall signatures span 2 order of magnitudes in mass, and the virial parameter varies in the range $0.10 \leq \alpha_{vir} \leq 1.96$, similar to the α_{vir} distribution of the rest of the sample, with four clumps that have $\alpha_{vir} \geq 1$. The differences between these clumps and the sub-sample of clumps with no blue-asymmetric HCO^+ spectra are not statistically significant. A Kosmogorov-Smirnov test, which gives the probability that two samples come from the same distribution, gives a 71% probability that the distribution of the virial parameter of infalling clumps is similar to that of the other clumps. A t-Student test, which gives the probability that two samples have the same mean, gives a probability of 61% that the means of the virial parameter distributions in the two sub-samples are the same.

In Figure 11 we show the α_{vir} vs. mass diagrams for the 21 clumps with blue-asymmetric HCO^+ spectra (upper panel) and for the remaining 192 clumps (lower panel), with the respective fits. The linear fits in the diagrams in Figure 11 have very similar slopes within the uncertainties, suggesting that the observed values of the virial parameter are independent of the dynamics of the clumps.

6.1 Properties of infalling gas

Clumps with double-peaked blue-asymmetric spectra can be modeled to obtain properties such as the infall velocity v_{in} and mass accretion rate \dot{M} using e.g. the two-layers model of Myers et al. (1996). In this model the line intensity of the red and blue peaks, as well as of the dip in correspondence of the central velocity of the clump (deduced from an optically thin line such as N_2H^+) are used to estimate the infall velocity:

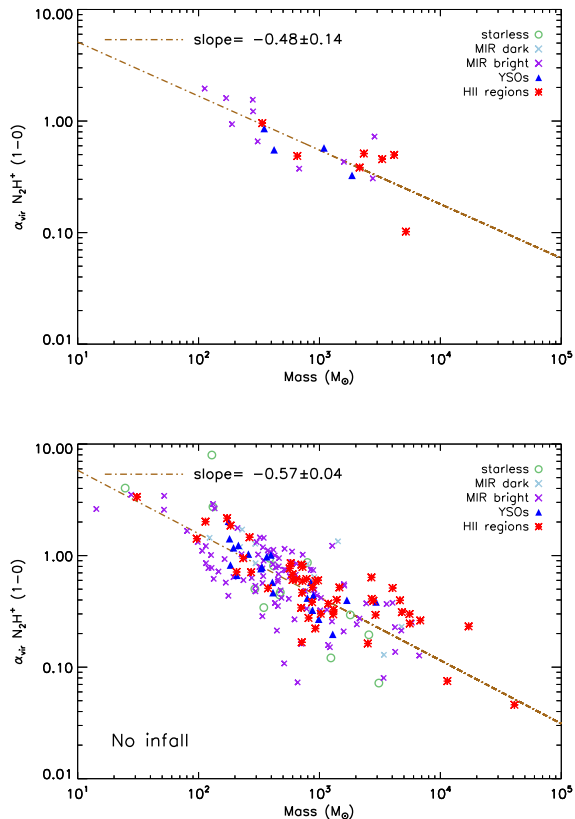


Figure 11. Upper panel: α_{vir} vs. mass diagram for the 21 clumps with evidence of infalling motions in their $\text{HCO}^+ (1-0)$ spectra. Lower panel: same diagram for the remaining 192 clumps of the sample. The slopes of the best linear fit in the two plots are the same within the uncertainties, suggesting that the clumps dynamics is independent of the values of α_{vir} .

$$v_{in} = \frac{\sigma^2}{v_{red} - v_{blue}} \ln \left(\frac{1 + e^{(T_{blue} - T_{dip})/T_{dip}}}{1 + e^{(T_{red} - T_{dip})/T_{dip}}} \right). \quad (4)$$

where v_{red} and v_{blue} are the velocities of the blue and red peaks respectively, T_{blue} and T_{red} are the main beam temperatures of the blue and red peaks respectively and T_{dip} is the main beam temperature of the valley between the two peaks. To obtain these parameters, the spectra of the 21 clumps have been fitted with a double-Gaussian model using the `mpfitfun` IDL routine (Markwardt 2009). The spectra with the double-Gaussian fits are in Appendix C.

The infall velocity varies in the range $0.03 \leq v_{in} \leq 2.75 \text{ km s}^{-1}$, with an average value of $v_{in} = 0.55 \text{ km s}^{-1}$, in line with similar estimates in massive star forming regions (Fuller, Williams & Sridharan 2005; Rygl et al. 2013; Traficante et al. 2017). The value for each clump is in Table 4.

The mass accretion rate \dot{M} can be evaluated assuming spherical geometry as $\dot{M} = 4\pi R^2 n_{\text{H}_2} \mu m_{\text{H}} v_{in}$ (Myers et al. 1996), where m_{H} is the hydrogen mass, $\mu = 2.33$ is the molecular weight and n_{H_2} the volume density. It ranges in the limits $0.68 \leq \dot{M} \leq 45.8 \times 10^{-3} M_{\odot} \text{ yr}^{-1}$ (Table 4), with an average value of $\dot{M} = 9.6 \times 10^{-3} M_{\odot} \text{ yr}^{-1}$, comparable with similar results for massive protostellar clumps (e.g. Rygl et al. 2013; Peretto et al. 2013).

In Table 5 we show the average values of v_{in} and \dot{M} for the various evolutionary phases. There is an indication that \dot{M} is higher in HII regions than in the rest of the sample, suggesting an increasing of the accretion rate with evolution. Since we do not observe

Clump	v_{in} (km s ⁻¹)	\dot{M} (10 ⁻³ M _⊙ yr ⁻¹)	ϵ
G309.422-00.622	1.01(0.51)	7.22(4.33)	0.11(0.08)
G316.085-00.674	0.26(0.13)	0.68(0.41)	8.80(6.60)
G316.140-00.504	0.85(0.43)	28.65(17.19)	0.15(0.11)
G320.285-00.309	0.53(0.27)	11.90(7.14)	3.08(2.31)
G321.935-00.007	0.26(0.13)	1.63(1.98)	11.39(8.54)
G322.520+00.637	0.22(0.11)	1.27(0.76)	10.81(8.11)
G327.393+00.199	0.19(0.10)	2.45(1.47)	41.37(31.03)
G327.403+00.444	0.66(0.33)	17.11(10.27)	1.50(1.13)
G331.132-00.245	0.21(0.11)	6.11(3.67)	87.48(65.61)
G331.708+00.583	0.55(0.28)	9.65(5.79)	3.80(2.85)
G331.723-00.203	0.74(0.37)	4.23(2.54)	0.65(0.49)
G332.604-00.168	0.21(0.11)	0.73(0.44)	21.47(16.10)
G338.927+00.632	1.43(0.72)	45.83(27.50)	0.15(0.11)
G339.476+00.185	1.51(0.76)	36.06(21.64)	0.17(0.13)
G339.924-00.084	0.51(0.26)	9.21(5.53)	1.60(1.20)
G341.215-00.236	0.20(0.10)	1.73(1.04)	16.45(12.34)
G342.822+00.382	0.33(0.17)	3.87(2.32)	4.26(3.20)
G343.520-00.519	0.33(0.17)	2.13(1.28)	5.39(4.04)
G343.756-00.163	0.23(0.12)	3.30(1.98)	14.20(10.65)
G344.101-00.661	1.13(0.57)	7.00(4.20)	0.30(0.23)
G344.221-00.594	0.24(0.12)	1.61(0.97)	15.72(11.79)

Table 4. Parameters of the 21 clumps derived from double-peaked, blue-shifted HCO⁺ (1 – 0) spectra. Col.1: Clump name; Col. 2: Infall velocity; Col. 3: Mass accretion rate; Col. 4: Efficiency. The uncertainties have been propagated from the uncertainties on M, R and σ showed in Table 1, assuming a further uncertainties of 25% on the estimation of v_{red} and v_{blue} due to the resolution of the smoothed spectra used to estimate the velocities (see Section 2.4). We obtained uncertainties of 50%, 60% and 75% to the estimation of v_{in} , \dot{M} and ϵ respectively.

Clump phase	Count	\bar{v}_{in} (km s ⁻¹)	$\bar{\dot{M}}$ (10 ⁻³ M _⊙ yr ⁻¹)
24 μ m bright	10	0.54	7.82
YSOs	4	0.51	5.25
HII regions	7	0.60	14.74

Table 5. Mean infall parameters of the 21 clumps with infall signatures divided by different evolutionary phases. Col.1: Clump evolutionary phase; Col 2: number of clumps in each phase; Col. 3: Mean infall velocity; Col. 4: Mean mass accretion rate.

clumps at the earliest evolutionary stages with clear hint of infall motions in our data, in order to investigate this trend we have combined our data with the sample of seven 70 μ m quiet massive clumps studied in Traficante et al. (2017), for which they have measured the mass accretion rates. In Figure 12 we plot \dot{M} against the quantity L/M. There is a large scatter among the sources, but the correlation is not irrelevant ($\rho = 0.44$). With an average accretion rate for the 70 μ m quiet clumps of 0.91×10^{-3} M_⊙ yr⁻¹, this diagram support the indication that \dot{M} increases with evolution in these massive objects.

The mass accretion rate is instead proportional to the surface density ($\rho = 0.61$), as showed in Figure 13. This result implies that higher density regions sustain a higher accretion rate, a point that we will further discuss in Section 7.2.

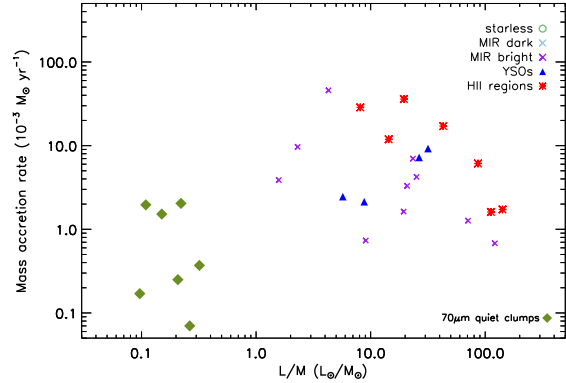


Figure 12. Mass accretion rate as function of the L/M ratio, an indicator of clumps evolution. Our sample of 21 clumps has been combined with the survey of 70 μ m quiet clumps in Traficante et al. (2017, green diamonds). Altogether, these data show a moderate correlation ($\rho = 0.44$) and suggest that the mass accretion rate may increase with evolution.

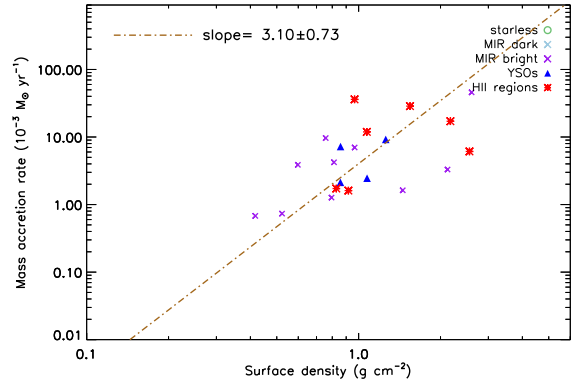


Figure 13. Mass accretion rate as function of surface density. The Pearson's correlation coefficient is 0.61, suggesting a good correlation between these two quantities. The best-fit gives a slope of 3.10 ± 0.73 , suggesting an increasing of \dot{M} as function of Σ .

7 ORIGIN OF NON-THERMAL MOTIONS

In comparison with the non-thermal motions found in GMCs, our clumps have an excess of kinetic energy at small radii (Figure 4), in agreement with the findings of Ballesteros-Paredes et al. (2011, and references therein). Larson (1981) himself noted that the relation breaks down at the size of the clumps/cores and the inner part of massive star forming regions tends to have higher velocity dispersion at a given radius. The kinetic energy excess in this ensemble of clumps should have a different origin from shock turbulence. In this Section we investigate possible origins of the observed non-thermal motions in these objects.

A possible explanation for the origin of non-thermal motions in massive clumps is given by the model of Murray & Chang (2015). These authors break down the assumption that collapsing regions are in hydrostatic equilibrium. Instead, the turbulent velocity is adiabatically heated by the collapse itself, following the evolution of the system. Combined with the back-pressure generated by turbulence, Murray & Chang (2015) predicted a power-law form for the Larson's first relation of $R_{cc} \propto \sigma^{0.2-0.3}$. This model

successfully predicts a deviation of Larson's first relation in massive star forming regions as found by e.g. Caselli & Myers (1995) and Shirley et al. (2003). However our observations, in agreement with the findings of Ballesteros-Paredes et al. (2011) and Traficante et al. (2018), suggest that there is no correlation between velocity dispersion and size of an ensemble of clumps.

Non-thermal motions in massive star forming objects may also be driven by stellar feedbacks such as protostellar jets/outflows (e.g. Federrath 2016). Figures 4 and 5 show, however, that the velocity dispersion in starless clumps, the less affected by stellar feedbacks, is similar to the one observed in more evolved clumps, and the quantity $\sigma/R^{0.5}$ is not constant. Even if stellar feedbacks play an important role in the observed non-thermal motions of protostars, it cannot alone explain the observed linewidth-size relation in all these clumps.

7.1 Accretion-driven turbulence

An alternative explanation to the observed supersonic motions is that these non-thermal velocities are the result of accretion-driven turbulence (Klessen & Hennebelle 2010). This model predicts that (at least part of) the energy injected by the accretion into the system is converted into turbulent motions, which set up a Kolmogorov-like turbulent cascade. The large-scale fed accretion generates enough turbulence to produce supersonic motions in the high-density clumps.

If the energy injected by the infall motions is much lower than the turbulent dissipation rate, the conversion of these motions into turbulent energy cannot maintain the turbulent cascade which will rapidly dissipate. The observed non-thermal motions would therefore not be the result of a turbulent cascade, and they would not follow a Larson-like relation.

The key parameters to evaluate the energy injected by the accretion and the turbulent dissipation rate are the scale at which the turbulence is driven and the mass of the infalling gas. We consider that the clumps are globally collapsing as a whole (as observed in e.g. Traficante et al. 2017), and the representative scale is the scale of the clumps.

With these assumptions, the turbulent dissipation rate is $\dot{E}_{dis} = \frac{1}{2}M\sigma^2/\tau_d = \frac{1}{2\sqrt{3}L_d}M\sigma^3$ (Hennebelle & Falgarone 2012), where M is the total mass of the clump. The turbulence decays in a turbulent crossing time $\tau_d = L_d/\sigma_{3D}$, with $\sigma_{3D} = \sqrt{3}\sigma$ being the 3-dimensional velocity dispersion and L_d , the turbulence driving scale (Hennebelle & Falgarone 2012, and references therein), the size of the clump. The energy injected by the accretion is $\dot{E}_{inj} = \frac{1}{2}\dot{M}v_{in}^2$ (Klessen & Hennebelle 2010), where \dot{M} has been evaluated from the mean density of the clumps as in Section 6.1. Defining the efficiency $\epsilon = \dot{E}_{dis}/\dot{E}_{inj}$, the conditions for accretion-driven turbulence are satisfied if $\epsilon \leq 1$ (Klessen & Hennebelle 2010).

We evaluate \dot{E}_{dis} , \dot{E}_{inj} and ϵ for the 21 clumps with defined infall velocities (Section 6.1). The efficiency as function of the infall velocity is in Figure 14. The efficiency goes rapidly down as the infall velocity increases, and becomes less than 1 for the six clumps with the highest accretion rates and with infall velocities $v_{in} \geq 0.75$ km s⁻¹ (Table 4). For the majority of the clumps the turbulent dissipation rate seems to be sufficiently high to dissipate the energy injected by the accretion.

The observed non-thermal motions can partly originate from turbulence driven by the accretion in clumps with high infall velocity and accretion rates, but, under the hypothesis that the driving scales are the clump scales that are globally collapsing as a whole,

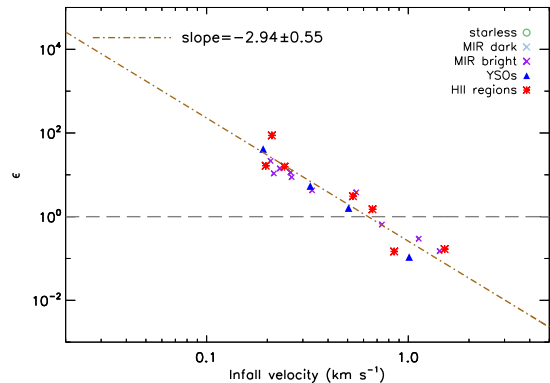


Figure 14. Efficiency ϵ as function of the infall velocity. The red-dashed line is the best-fit to the data and shows that the efficiency goes rapidly down with the increase of the infall velocity. The black dashed line is in correspondence of $\epsilon = 1$. The non-thermal motions observed in clumps with efficiency below this value may be due to accretion driven turbulence.

this mechanism alone cannot explain the supersonic non-thermal motions observed in clumps with infall velocity $v_{in} < 0.75$ km s⁻¹.

7.2 Gravity-driven non-thermal motions

Non-thermal motions in star forming regions may originate from gravity itself, which seems to play a dominant role in the evolution of molecular clouds able to form high-mass stars, down to ≈ 0.1 pc scales (Li & Burkert 2016, 2017). In particular, non-thermal motions may originate from a hierarchical, global collapse of clouds and clumps (Ballesteros-Paredes et al. 2011). In this picture the supersonic motions are not hydrodynamical turbulence, but organized motions driven by gravity in multiple centers of collapse. This hypothesis implies that massive regions should develop a larger velocity dispersion for larger column densities (Ballesteros-Paredes et al. 2011), which may also explain the higher accretion rates observed in higher surface density clumps (Figure 13).

In Figure 15 we show the σ vs. Σ diagram. The correlation is not strong, but there is a weak positive correlation ($\rho = 0.30$) and regions with higher surface density have on average higher velocity dispersion, suggesting that non-thermal motions may partly result from the large gravitational force acting in the system.

This model also considers that the system develops a Heyer-like relation $\sigma/R^{1/2} \propto \Sigma^{1/2}$ (Heyer et al. 2009). This relation is equivalent to a generalized first Larson's relation for regions with different surface densities (Ballesteros-Paredes et al. 2011; Camacho et al. 2016). In this global collapse model, rather than the virial equilibrium what counts is the conservation of the total energy of the system. The virial parameter represents energy equipartition, which numerically is equivalent to set $\alpha_{eq} = 2$ (Ballesteros-Paredes et al. 2011).

The Heyer plot for our clumps is in Figure 16. The correlation between Σ and the quantity $\sigma/R^{1/2}$ is relatively weak ($\rho = 0.18$). The majority of the clumps lie below the equipartition value and there is a significant spread across the diagram, which reflects the different values of the virial parameter (Section 4.2).

In Figure 17 we show the same Heyer plot, but limited to clumps with mass $M \geq 1000 M_{\odot}$. The correlation in this case is higher ($\rho = 0.40$). We interpret this result as an indication that

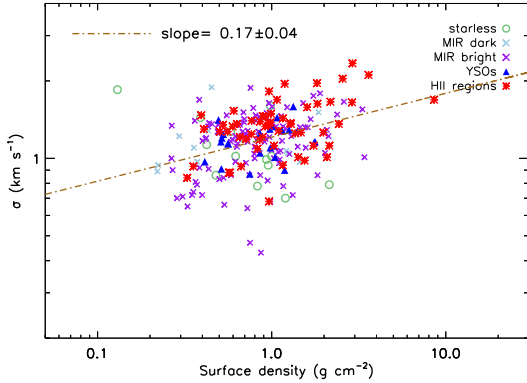


Figure 15. Velocity dispersion σ as function of surface density Σ . The positive correlation is weak, with a Pearson’s correlation coefficient of $\rho = 0.30$, and the best-fit gives a slope of 0.17 ± 0.04 .

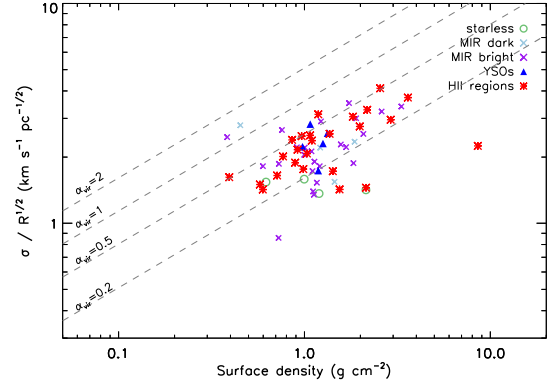


Figure 17. Same as in Figure 16 but for clumps with $M \geq 1000 M_{\odot}$. The correlation is higher, with a Pearson’s coefficient of $\rho = 0.40$.

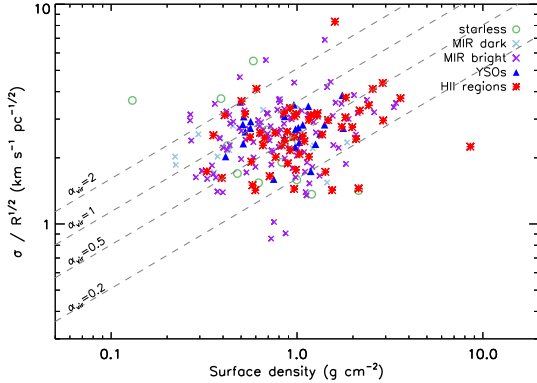


Figure 16. Heyer plot, i.e. the quantity $\sigma/R^{1/2}$ versus the surface density Σ . The dashed lines are in correspondence of constant values of the virial parameter, from $\alpha_{vir}=2$ (highest line) to $\alpha_{vir}=0.2$ (lowest line). The correlation is weak, the Pearson’s coefficient is $\rho = 0.18$.

gravity drives at least partially the observed non-thermal motions, in particular in the more massive clumps of the sample. If gravity contributes to the generation of the observed kinetic energy, this contribution is more dominant at higher masses, although all these massive clumps lie below the equipartition value. A possible explanation for the observed departure from the equipartition, at least for the sub-virial clumps at the earliest phases of evolution, is that a collapsing region with sufficiently low level of local turbulence can start in a sub-virial state, and it can reach the equipartition during its evolution (Ballesteros-Paredes et al. 2017). As discussed in Section 5, there may also be a fraction of kinetic energy not properly traced in these massive regions, which may explain the departure from the energy equipartition expected from the models. In the next Section we explore if the magnetic pressure in these clumps is another valid explanation for this observed departure.

7.3 Role of magnetic fields

In this Section we estimate the possible contribution of the magnetic fields to the stability of these clumps.

In accordance with the findings of the previous Section these

clumps, in particular the more massive ones, may be undergoing gravitational collapse. However, these clumps may be sustained against the collapse by strong magnetic pressure.

Crutcher (2012) showed that, observationally, the magnetic fields strength may not be sufficient to balance gravity in high density regions ($n \geq 300 \text{ cm}^{-3}$), although they may give a significant contribution in lower density ones. There is an expected upper limit to the intensity of the magnetic fields B_{Cr} which increases at increasing density as $B_{Cr} \approx \Sigma^{0.65}$ (Crutcher 2012). At the same time, the work of Kauffmann, Pillai & Goldsmith (2013) showed that the magnetic fields strength required to maintain a clump in a hydrostatic equilibrium (equivalent to $\alpha_{vir}=2$) is proportional to the observed non-thermal motions following the relation:

$$B_{MBE} = 81 \mu\text{G} \frac{M_{\phi}}{M_{BE}} \left(\frac{\sigma}{\text{kms}^{-1}} \right)^2 \left(\frac{R}{\text{pc}} \right)^{-1} \quad (5)$$

where M_{ϕ}/M_{BE} is the ratio between the magnetic flux mass and mass of sphere in hydrostatic equilibrium (a Bonnor-Ebert sphere), and it is proportional to $2/\alpha_{vir}-1$ (Kauffmann, Pillai & Goldsmith 2013).

In Figure 18 we show the quantity $B_{ratio}=B_{MBE}/B_{Cr}$ as function of the surface density for the 199 clumps with $\alpha_{vir} \leq 2$. Almost 40% of these clumps (80) lies below the threshold $B_{ratio} = 1$. The majority of them have $B_{ratio} > 1$, for which the implication is that only exceptionally high magnetic fields can stabilize their collapse.

In Figure 19 we show B_{ratio} as function of the mass of the clumps. The correlation is strong ($\rho = 0.80$). This diagram shows that the intensity of the magnetic fields required to stabilize a collapsing clump exceeds the threshold estimated by Crutcher (2012) if the clump has a mass $M \geq 1000 M_{\odot}$.

The results suggest that magnetic fields may be relevant in some of these clumps but for the majority of them, in particular the more massive ones, this mechanism alone cannot sustain the collapse at clump scales. This analysis does not exclude that at the scales of the inner cores the magnetic fields may play a relevant role and act against the gravitational collapse (e.g. Fontani et al. 2016). Further observations at high resolution with instruments like ALMA or NOEMA are required to investigate the properties of these clumps at the core scales.

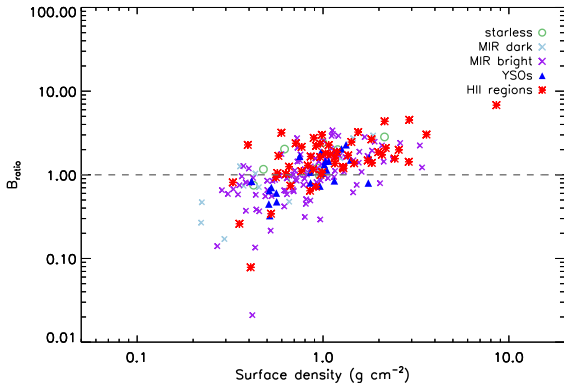


Figure 18. $B_{ratio} = B_{MBE} / B_{Cr}$ ratio as function of surface density. To be stabilized by magnetic fields, clumps with $B_{ratio} > 1$ (black dotted line) requires magnetic fields stronger than the maximum values estimated by Crutcher (2012).

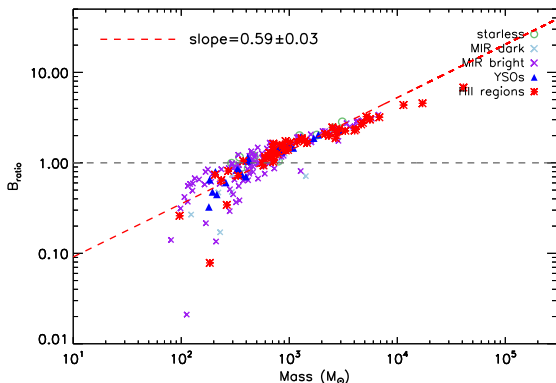


Figure 19. B_{ratio} as function of the clump mass. The correlation is strong (Pearson's coefficient $\rho = 0.80$) and shows that the magnetic fields required to stabilize the clumps increase significantly with the mass of the clumps. For $M \geq 1000 M_{\odot}$ exceptionally high magnetic fields are required to slow down the collapse.

8 CONCLUSIONS

We have discussed the validity of the three Larson's relations and the implications of the results for a large sample of 213 massive clumps at different evolutionary stages. These clumps have been obtained combining the Hi-GAL clumps catalogue (Elia et al. 2017) with the MALT90 survey of 3mm emission lines (Jackson et al. 2013) and selected to be a sample of sources with well-known distances, dust emission properties and N_2H^+ (1 – 0) emission, the latter used to extract the gas kinematics. The sample has been divided in five evolutionary stages, and we have obtained: 14 starless, 12 protostar MIR dark, 106 protostar MIR bright, 25 YSOs, and 56 HII regions. They are all located in the IV Quadrant and the vast majority of these clumps will likely form high-mass stars, based on the Kauffmann, Pillai & Goldsmith (2013) and Baldeschi et al. (2017) massive star formation selection criteria.

We have shown that the three Larson's relations do not describe the properties of an ensemble of massive clumps, independently from the evolutionary stage of these objects. At these scales σ is not proportional to the radius R (first Larson's relation), these

clumps are not in virial equilibrium (second Larson's relation), and these clumps have no constant surface density (third Larson's relation).

We demonstrated that the absence of a scaling relation between σ and R implies that the virial parameter α_{vir} , defined as the ratio between kinetic energy E_{kin} and gravitational energy E_G , decreases with mass and radius only as function of the gravitational content of the clumps, independently of their kinetic energy.

A consequence of these findings is that the measured virial parameter is not a good descriptor of the clumps dynamics. In fact, the virial values in clumps with evidence of infalling motions (measured from blue-asymmetric HCO^+ (1 – 0) spectra) are statistically indistinguishable from the values of the rest of the sample. This also suggests that all these clumps may be dynamically active, even the ones without clear evidence in their HCO^+ (1 – 0) spectra.

We showed that the observed non-thermal motions in massive clumps are not likely due to turbulent cascade, collapse in adiabatically heated regions, nor accretion-driven turbulence. The velocity dispersion and mass accretion rate moderately correlate with surface density, which suggest that the gravitational collapse contribute at least partially at the variation of the observed non-thermal motions, in agreement with global collapse models (Ballesteros-Paredes et al. 2011). The gravitational collapse seems to play a dominant role particularly in the more massive clumps of our sample ($M \geq 1000 M_{\odot}$), although they all are sub-virial and not in energy equipartition as predicted in many gravitationally-driven collapse models.

We also showed that, on average, magnetic fields may not contribute significantly to the stability of these clumps, and exceptionally strong magnetic fields would be required to stabilize the clumps with $M \geq 1000 M_{\odot}$.

ACKNOWLEDGEMENTS

AT wants to thanks J. Kauffmann for the useful and stimulating discussions that lead to some of the results in this work. This work has benefited from research funding from the European Community's Seventh Framework Programme. ADC acknowledges the support of the UK STFC consolidated grant ST/N000706/1.

REFERENCES

- Baldeschi A., Elia D., Molinari S., et al., 2017, MNRAS, 466, 3682
- Ballesteros-Paredes J., 2006, MNRAS, 372, 443
- Ballesteros-Paredes J., Hartmann L. W., Vázquez-Semadeni E., et al., 2011, MNRAS, 411, 65
- Ballesteros-Paredes J., Vázquez-Semadeni E., Palau A., et al., 2017, arXiv.org, arXiv:1710.07384
- Beckwith S. V. W., Sargent A. I., Chini R. S., et al., 1990, AJ, 99, 924
- Bertoldi F., McKee C. F., 1992, ApJ, 395, 140
- Bonnell I. A., Vine S. G., Bate M. R., 2004, MNRAS, 349, 735
- Brand J., Blitz L., 1993, A&A, 275, 67
- Camacho V., Vázquez-Semadeni E., Ballesteros-Paredes J., et al., 2016, ApJ, 833, 113
- Caselli P., Myers P. C., 1995, ApJ, 446, 665
- Chira R. A., Smith R. J., Klessen R. S., et al., 2014, MNRAS, 444, 874
- Crutcher R. M., 2012, ARAA, 50, 29

- Csengeri T., Urquhart J. S., Schuller F., et al., 2014, *A&A*, 565, A75
- Egan M. P., Price S. D., Kraemer K. E., 2003, *AAS* 203, 203, 57.08
- Elia D., Molinari S., Schisano E., et al., 2017, *MNRAS*, 471, 100
- Ellsworth-Bowers T. P., Glenn J., Riley A., et al., 2015, *ApJ*, 805, 157
- Federrath C., 2016, *JP*, 719, 012002
- Fontani F., Commerçon B., Giannetti A., et al., 2016, *A&A*, 593, L14
- Fuller G. A., Williams S. J., Sridharan T. K., 2005, *A&A*, 442, 949
- Griffin M., Swinyard B., Vigroux L., et al., 2008, in *SPIE Conference Series*, Vol. 7010
- Gutermuth R. A., Heyer M., 2015, *ApJ*, 149, 64
- He Y.-X., Zhou J.-J., Esimbek J., et al., 2015, *MNRAS*, 450, 1926
- Hennebelle P., Falgarone E., 2012, *A&AR*, 20, 55
- Heyer M. H., Brunt C. M., 2004, *ApJ*, 615, L45
- Heyer M. H., Krawczyk C., Duval J., et al., 2009, *ApJ*, 699, 1092
- Hoare M. G., Kurtz S. E., Lizano S., et al., 2007, *Protostars and Planets V*, 181
- Hou L. G., Han J. L., Shi W. B., 2009, *A&A*, 499, 473
- Jackson J., Rathborne J., Foster J. B., et al., 2013, *PASA*, 30, e057
- Jackson J. M., Rathborne J. M., Shah R. Y., et al., 2006, *ApJS*, 163, 145
- Juvela M., Demyk K., Doi Y., et al., 2015, *A&A*, 584, A94
- Kauffmann J., Pillai T., 2010, *ApJ*, 723, L7
- Kauffmann J., Pillai T., Goldsmith P. F., 2013, *ApJ*, 779, 185
- Kauffmann J., Pillai T., Shetty R., et al., 2010, *ApJ*, 716, 433
- Kegel W. H., 1989, *A&A*, 225, 517
- Klessen R. S., Hennebelle P., 2010, *A&A*, 520, A17
- König C., Urquhart J. S., Csengeri T., et al., 2017, *A&A*, 599, A139
- Kritsuk A. G., Lee C. T., Norman M. L., 2013, *MNRAS*, 436, 3247
- Larson R. B., 1981, *MNRAS*, 194, 809
- Lee Y.-N., Hennebelle P., 2016, *A&A*, 591, A30
- Li G.-X., Burkert A., 2016, *MNRAS*, 461, 3027
- Li G.-X., Burkert A., 2017, *MNRAS*, 464, 4096
- Lombardi M., Alves J., Lada C. J., 2010, *A&A*, 519, L7
- Lumsden S. L., Hoare M. G., Urquhart J. S., et al., 2013, *ApJS*, 208, 11
- Mac Low M.-M., Klessen R. S., 2004, *Reviews of Modern Physics*, 76, 125
- Markwardt C. B., 2009, in *ASPC*, Vol. 411, *ADASS XVIII*, Bohlender D. A., Durand D., Dowler P., eds., p. 251
- McKee C. F., Ostriker E. C., 2007, *ARAA*, 45, 565
- McKee C. F., Tan J. C., 2003, *ApJ*, 585, 850
- Miettinen O., 2014, *A&A*, 562, A3
- Molinari S., Merello M., Elia D., et al., 2016a, *ApJL*, 826, L8
- Molinari S., Pezzuto S., Cesaroni R., et al., 2008, *A&A*, 481, 345
- Molinari S., Schisano E., Elia D., et al., 2016b, *A&A*, 591, A149
- Molinari S., Schisano E., Faustini F., et al., 2011, *A&A*, 530, A133
- Molinari S., Swinyard B., Bally J., et al., 2010, *PASP*, 122, 314
- Murray N., Chang P., 2015, *ApJ*, 804, 44
- Myers P. C., Mardones D., Tafalla M., et al., 1996, *ApJL*, 465, L133
- Ossenkopf V., Henning T., 1994, *A&A*, 291, 943
- Padoan P., Nordlund Å., 2002, *ApJ*, 576, 870
- Paradis D., Veneziani M., Noriega-Crespo A., et al., 2010, *A&A*, 520, L8+
- Peretto N., Fuller G. A., Duarte-Cabral A., et al., 2013, *A&A*, 555, A112
- Plume R., Jaffe D. T., Evans N. J. I., et al., 1997, *ApJ*, 476, 730
- Poglitsch A., Waelkens C., Geis N., et al., 2010, *A&A*, 518, L2+
- Ragan S. E., Bergin E. A., Gutermuth R. A., 2009, *ApJ*, 698, 324
- Reid M. J., Menten K. M., Zheng X. W., et al., 2009, *ApJ*, 700, 137
- Russeil D., Pestalozzi M., Mottram J. C., et al., 2011, *A&A*, 526, A151
- Rygl K. L. J., Wyrowski F., Schuller F., et al., 2013, *A&A*, 549, A5
- Schuller F., Menten K. M., Contreras Y., et al., 2009, *A&A*, 504, 415
- Shirley Y. L., Evans N. J. I., Young K. E., et al., 2003, *ApJSS*, 149, 375
- Smith R. J., Shetty R., Beuther H., et al., 2013, *ApJ*, 771, 24
- Solomon P. M., Rivolo A. R., Barrett J., et al., 1987, *ApJ*, 319, 730
- Svoboda B. E., Shirley Y. L., Battersby C., et al., 2016, *ApJ*, 822, 59
- Tan J. C., Beltrán M. T., Caselli P., et al., 2014, *Protostars and Planets VI*, 149
- Traficante A., Fuller G., Smith R. J., et al., 2018, *MNRAS*, 473, 4975
- Traficante A., Fuller G. A., Billot N., et al., 2017, *MNRAS*, 470, 3882
- Traficante A., Fuller G. A., Peretto N., et al., 2015a, *MNRAS*, 451, 3089
- Traficante A., Fuller G. A., Pineda J. E., et al., 2015b, *A&A*, 574, A119
- Urquhart J. S., König C., Giannetti A., et al., 2018, *MNRAS*, 473, 1059
- Urquhart J. S., Moore T. J. T., Csengeri T., et al., 2014, *MNRAS*, 443, 1555
- Whitaker J. S., Jackson J. M., Rathborne J. M., et al., 2017, *AJ*, 154, 140
- Wood D. O. S., Churchwell E., 1989, *ApJSS*, 69, 831
- Wright E. L., Eisenhardt P. R. M., Mainzer A. K., et al., 2010, *ApJ*, 140, 1868
- Wu J., Evans N. J. I., Shirley Y. L., et al., 2010, *ApJS*, 188, 313
- Wyrowski F., Güsten R., Menten K. M., et al., 2016, *A&A*, 585, A149
- Zinnecker H., Yorke H. W., 2007, *ARA&A*, 45, 481

APPENDIX A: ALTERNATIVE SOURCE PHOTOMETRY

In order to estimate the uncertainties associated with the chosen source extraction and photometry strategy described in Elia et al. (2017) and obtained using the *Cutex* algorithm (Molinari et al. 2011), we compared the results with the photometry obtained using an alternative method.

The alternative photometry has been done using *Hyper*, which performs elliptical aperture photometry in presence of highly variable backgrounds (Traficante et al. 2015b). The 2 FWHMs and the position angle of the clumps in the Elia et al. (2017) catalogue, estimated from the 250 μm fit, have been used to define the radius of the ellipses over which perform the *Hyper* aperture photometry at all wavelengths. This approach is substantially different from the method used in the Hi-GAL catalogue, since *Cutex* estimates the flux as the integral of the 2d-Gaussian fitted at each wavelength.

The flux differences in percentage at each wavelength are in Figure A1.

As expected, at the reference wavelength of $250\ \mu\text{m}$ the flux differences are minimal. At $\lambda < 250\ \mu\text{m}$ the *Cutex* fluxes are lower than the *Hyper* counterparts on average. This is particularly true at $160\ \mu\text{m}$, where the diffuse emission contributes substantially to the integrated flux. At $70\ \mu\text{m}$ the measured emission is dominated by the emission from the central protostars, and the differences are less sensitive to the photometry method. At $\lambda > 250\ \mu\text{m}$ the *Cutex* fluxes are re-scaled according to the $250\ \mu\text{m}$ size in the Hi-GAL catalogue (Elia et al. 2017), leading to a small differences between the *Hyper* and *Cutex* photometry.

In order to add an additional point in the SED fitting, for each source we also extracted the fluxes at $870\ \mu\text{m}$, evaluated from the ATLASGAL calibrated maps using the same aperture adopted to extract the Hi-GAL fluxes.

Few sources (21) are saturated at $250\ \mu\text{m}$ in the Hi-GAL maps. This is due to a combination of the strong flux emission of some sources whose SED peaks at around the $160\text{-}250\ \mu\text{m}$ wavelengths, and of the higher dynamical range of the PACS instrument at $160\ \mu\text{m}$ which allows the $160\ \mu\text{m}$ band to saturate at higher fluxes than the SPIRE bands. While these sources still have a flux estimation in the Hi-GAL catalogue, no aperture photometry can be reliably performed, and we excluded these clumps from the comparison. The source properties have been evaluated using the same greybody model described in Section 2. We obtained a final sample of 192 clumps with well-defined dust properties that we used for the comparison. The mass differences in percentage are showed in Figure A2.

To estimate the uncertainties on the mass due to the source photometry, we fit a Gaussian to the histogram of the mass differences. The standard deviation of the Gaussian is $\approx 25\%$, that we assume as mass uncertainties. Note that the masses estimated with *Hyper* are $\approx 10\%$ systematically lower than the *Cutex* counterparts, likely as consequence of the different photometry at $\lambda = 160\ \mu\text{m}$. This systematic offset however does not influence the main results of this work, as discussed in Section 2.4.

To further investigate this point, in Figure A3 we show the α_{vir} -mass diagram and the mass-radius diagram obtained from the results of the *Hyper* photometry. The values of the slopes α and δ are consistent with the values derived in Section 4.3. Also, the slope of the α_{vir} -mass diagram is still determined from the slope of the mass-radius diagram, according to Equation 2. Given a mass-radius slope of $\delta = 2.28 \pm 0.11$, the expected α_{vir} -mass slope would be $\alpha = -0.56 \pm 0.03$, in agreement with the result showed in Figure A2, $\alpha = -0.55 \pm 0.04$.

APPENDIX B: CLUMP PROPERTIES

APPENDIX C: HCO⁺ (1-0) SPECTRA

HCO⁺(1 – 0) spectra of the 21 clumps with double-peaked blue-asymmetries. The red lines in the plot are the double-Gaussian fits,

and the blue crosses are the positions of the 2 identified peaks and in correspondence of the dip between the peaks.

G304.673+00.256	18:15:46.0	-16:39:08	0.23	19.9	229	6538	0.29	1.2	1.7	MIR dark
G305.095+00.250	18:16:00.6	-16:04:45	0.26	14.5	474	439	0.48	0.9	0.5	starless
G305.137+00.068	18:27:09.6	-12:42:37	0.41	17.0	4219	1738	1.68	1.4	0.2	MIR bright
G305.196+00.033	18:26:00.4	-11:52:21	0.45	27.9	2789	273915	0.92	1.4	0.4	HII region
G305.201+00.227	13:05:31.2	-62:29:59	0.46	18.2	1424	2854	0.45	1.9	1.3	MIR dark
G305.562+00.014	13:05:38.9	-62:14:40	0.34	31.1	1685	54175	0.98	1.3	0.4	YSO
G305.822-00.114	13:06:34.3	-62:33:49	0.28	18.7	1155	3216	1.00	1.1	0.3	MIR bright
G307.560-00.587	13:10:13.3	-62:32:33	0.39	32.1	2692	208376	1.19	1.9	0.6	HII region
G308.688+00.529	13:10:42.3	-62:43:16	0.27	12.9	1287	2580	1.19	0.9	0.2	YSO
G308.754+00.549	13:11:14.1	-62:45:05	0.35	23.2	795	19769	0.43	1.3	0.8	MIR dark
G309.116+00.139	13:11:16.7	-62:46:38	0.32	16.4	558	2777	0.37	0.8	0.4	MIR bright
G309.235-00.458	13:11:09.1	-62:33:25	0.19	14.2	709	1457	1.32	0.7	0.2	MIR bright
G309.382-00.134	13:14:26.8	-62:44:26	0.26	25.3	642	8596	0.66	1.4	0.8	MIR bright
G309.422-00.622	13:16:33.2	-62:49:42	0.18	17.8	421	11177	0.86	1.1	0.6	YSO
G310.014+00.390	13:16:43.6	-62:58:31	0.16	26.7	412	207612	1.05	1.0	0.5	YSO
G310.373-00.303	13:16:48.7	-62:50:36	0.23	15.8	781	1088	1.03	1.0	0.3	MIR bright
G311.044+00.687	13:17:15.7	-62:42:24	0.18	15.9	295	1054	0.58	0.9	0.5	MIR bright
G311.511-00.455	13:32:31.2	-63:05:17	0.15	23.2	183	27953	0.51	0.9	0.8	YSO
G311.556+00.331	13:36:32.6	-62:49:04	0.52	13.6	4027	1346	1.00	1.6	0.4	MIR bright
G311.627+00.265	13:40:27.1	-61:47:47	0.23	21.2	529	6741	0.69	1.2	0.7	MIR bright
G312.070+00.081	13:40:58.0	-61:45:43	0.08	24.8	52	4947	0.49	1.4	3.4	MIR bright
G312.330-00.088	13:44:39.9	-62:05:35	0.18	15.6	210	2129	0.43	1.3	1.8	MIR bright
G312.596+00.045	13:46:45.1	-62:38:58	0.29	29.9	1308	126752	1.03	1.1	0.3	HII region
G314.219+00.272	13:47:24.4	-62:18:07	0.34	39.5	1462	35723	0.86	1.4	0.5	HII region
G314.257+00.413	13:48:38.6	-62:46:08	0.25	16.5	387	1090	0.42	1.1	0.9	starless
G314.993+00.095	13:51:38.0	-61:39:08	0.14	19.1	80	1284	0.27	0.9	1.7	MIR bright
G316.085-00.674	13:56:01.7	-62:14:16	0.13	18.3	112	13664	0.42	1.2	2.0	MIR bright
G316.140-00.504	13:59:22.2	-61:06:30	0.47	20.9	5187	42134	1.54	1.0	0.1	HII region
G316.586-00.811	14:05:45.9	-62:04:50	0.15	21.6	180	4741	0.52	1.2	1.4	YSO
G316.779-00.098	14:04:16.0	-61:18:55	0.18	16.8	264	1186	0.53	1.4	1.5	ext. HII reg.
G317.408+00.110	14:04:22.4	-61:19:26	0.16	18.3	705	2972	1.74	1.1	0.3	ext. HII reg.
G317.467-00.067	14:04:59.4	-61:21:27	0.18	15.3	235	443	0.50	0.8	0.6	MIR bright
G317.701+00.110	14:08:58.2	-61:24:22	0.15	20.3	453	56352	1.30	1.2	0.6	MIR bright
G317.868-00.152	14:09:09.7	-61:24:21	0.14	20.8	426	1947	1.52	1.6	1.0	MIR bright
G318.050+00.087	14:08:49.6	-61:12:24	0.14	40.0	206	303692	0.67	0.9	0.7	HII region
G320.162+00.910	14:11:27.5	-61:29:23	0.17	11.4	445	144	0.98	0.7	0.2	MIR bright
G320.247+00.403	14:13:14.9	-61:16:52	0.21	18.0	1220	54661	1.84	0.9	0.2	MIR bright
G320.285-00.309	14:25:13.1	-60:31:41	0.45	25.0	3304	47480	1.07	1.7	0.5	HII region
G320.382+00.178	14:25:05.3	-60:22:52	0.87	16.5	6828	18366	0.60	1.3	0.3	ext. HII reg.
G321.380-00.300	14:26:26.5	-60:38:29	0.52	20.3	2908	33446	0.71	1.2	0.3	HII region
G321.756+00.029	14:31:34.8	-60:24:35	0.10	15.4	126	117	0.85	1.1	1.0	MIR bright
G321.935-00.007	14:39:06.0	-60:31:50	0.09	28.2	189	3678	1.45	1.3	0.9	MIR bright
G322.520+00.637	14:42:11.7	-60:41:02	0.16	19.6	308	21877	0.80	1.0	0.7	MIR bright
G323.444+00.094	14:42:02.2	-60:30:32	0.21	22.0	375	7890	0.57	0.9	0.5	HII region
G323.458-00.081	14:46:23.4	-60:35:47	0.23	31.5	929	164125	1.16	1.4	0.6	HII region
G324.200+00.120	14:45:20.1	-59:52:09	0.56	8.5	40990	370894	8.57	1.7	0.0	HII region
G324.923-00.570	14:45:17.6	-59:25:53	0.23	31.5	599	196146	0.77	1.2	0.7	HII region
G326.340+00.505	14:49:07.9	-59:24:44	0.30	15.9	727	501	0.55	1.5	1.0	MIR bright
G326.427+00.913	14:50:59.2	-59:50:09	0.17	16.6	346	582	0.83	0.8	0.3	starless
G326.449-00.749	14:50:09.5	-59:32:44	0.20	24.8	566	20554	0.97	1.4	0.8	HII region
G326.472-00.377	14:51:11.9	-59:16:59	0.19	27.5	724	247169	1.28	1.4	0.6	HII region
G326.566+00.197	14:53:16.8	-59:26:29	0.23	19.5	346	11734	0.44	1.4	1.4	MIR bright
G326.653+00.618	14:53:43.0	-59:08:50	0.23	13.5	794	482	0.98	1.6	0.9	starless
G326.657+00.594	15:00:55.4	-58:58:50	0.41	17.7	4635	41599	1.82	2.0	0.4	ext. HII reg.
G326.661+00.519	15:04:56.2	-57:25:28	0.14	23.7	334	11284	1.15	1.3	0.8	YSO
G326.671+00.554	15:11:01.7	-58:39:36	0.14	24.2	454	3557	1.61	1.3	0.6	MIR bright
G326.722+00.613	15:07:21.1	-57:49:21	0.18	25.0	643	49042	1.29	1.4	0.6	HII region
G326.754+00.603	15:10:18.8	-58:25:11	0.19	16.6	123	289	0.22	0.9	1.4	MIR dark
G326.772-00.125	15:09:05.1	-57:57:06	0.23	12.4	1270	5477	1.57	1.1	0.3	MIR bright
G326.781-00.242	15:09:41.4	-58:00:25	0.23	19.4	794	5268	1.03	1.1	0.4	YSO

Table B1. Properties of the 213 clumps analyzed in this work. Col. 1: Clump name; Col. 2-3: Clump coordinates; Col. 4: Clump radius, defined by the *Cutex* fit at $250\ \mu\text{m}$; Col. 5-7: Clump temperature, mass and luminosity as obtained from the SED fitting; Col. 8: Clump surface density; Col. 9: Velocity dispersion obtained from the N_2H^+ ($1-0$) emission; Col. 10: virial parameter. Col. 11: Clump evolutionary phase determined as discussed in Section 3.

Clump	RA ($^{\circ}$)	Dec ($^{\circ}$)	Radius (pc)	Temperature (K)	Mass (M_{\odot})	Luminosity (L_{\odot})	Σ (g cm^{-2})	σ km s^{-1}	α_{vir}	evol. phase
G326.795+00.382	15:11:54.4	-58:09:51	0.21	19.0	622	29026	0.95	0.8	0.3	MIR bright
G326.797+00.511	15:14:40.9	-58:11:49	0.30	12.1	583	151	0.42	1.2	0.9	MIR bright
G326.880-00.105	15:16:48.5	-58:09:48	0.16	17.9	133	10907	0.33	0.7	0.6	MIR bright
G326.919-00.305	15:17:23.0	-57:50:47	0.18	12.3	763	462	1.56	1.3	0.5	MIR bright
G326.975-00.030	15:18:26.5	-57:21:57	0.20	13.1	905	588	1.46	1.3	0.5	MIR bright
G326.987-00.031	15:19:43.0	-57:18:04	0.18	17.5	569	4530	1.16	1.3	0.7	MIR bright
G327.120+00.510	15:20:48.0	-56:26:42	0.22	36.8	396	201059	0.53	1.2	1.0	YSO
G327.167-00.356	15:28:31.5	-56:23:11	0.25	10.5	1596	363	1.74	1.8	0.6	MIR bright
G327.238-00.516	15:29:19.5	-56:31:21	0.21	14.1	341	584	0.49	1.3	1.2	MIR bright
G327.266-00.538	15:30:57.3	-56:15:00	0.18	25.5	146	4319	0.29	0.7	0.7	MIR bright
G327.272-00.574	15:32:51.8	-55:56:05	0.14	22.0	234	1032	0.85	1.2	0.9	HII region
G327.393+00.199	15:34:57.5	-55:27:24	0.26	22.9	1090	6232	1.07	1.4	0.6	YSO
G327.403+00.444	15:39:57.7	-56:04:10	0.26	29.6	2148	92426	2.17	1.7	0.4	HII region
G327.710-00.394	15:38:33.7	-55:27:56	0.25	17.5	1015	8302	1.09	1.1	0.3	MIR bright
G327.732-00.387	15:43:22.5	-54:21:33	0.26	16.7	2039	8855	2.08	1.3	0.2	MIR bright
G327.825-00.650	15:42:09.3	-53:58:47	0.23	21.8	388	38923	0.50	1.3	1.1	MIR bright
G327.947-00.113	15:49:18.7	-55:16:51	0.15	18.0	194	49642	0.56	1.1	1.2	YSO
G328.140-00.432	15:47:50.0	-54:58:31	0.19	25.6	195	3483	0.35	0.7	0.6	MIR bright
G328.256-00.413	15:45:53.2	-54:27:50	0.12	14.6	115	239	0.53	0.8	0.9	MIR bright
G328.899+00.350	15:43:36.1	-53:57:47	0.24	17.2	637	8804	0.70	1.2	0.7	MIR bright
G328.960+00.566	15:44:33.3	-54:05:25	0.61	22.6	5584	81472	0.99	1.4	0.2	HII region
G329.184-00.315	15:44:01.4	-53:58:45	0.18	40.0	131	186015	0.27	1.3	2.9	MIR bright
G329.422-00.164	15:44:35.3	-54:04:40	0.34	15.8	2509	19422	1.42	1.0	0.2	HII region
G329.467+00.516	15:44:42.9	-54:05:42	0.24	18.4	510	8577	0.58	1.2	0.7	MIR bright
G329.468+00.503	15:45:02.8	-54:09:06	0.16	28.2	238	61959	0.63	1.1	1.0	MIR bright
G329.524+00.084	15:44:57.2	-54:07:08	0.25	23.8	888	70965	0.94	1.5	0.7	MIR bright
G330.283+00.492	15:44:59.1	-54:02:18	0.28	23.0	782	22014	0.66	1.2	0.6	HII region
G330.673-00.375	15:45:12.0	-54:01:49	0.29	16.0	910	1873	0.73	1.2	0.5	MIR bright
G330.677-00.403	15:48:23.6	-54:35:28	0.22	19.5	725	4882	0.99	1.5	0.8	ext. HII reg.
G330.820-00.509	15:48:55.3	-54:40:39	0.27	12.2	428	1558	0.40	0.7	0.4	MIR bright
G330.876-00.384	15:46:20.8	-54:10:42	0.21	21.2	1303	124968	1.98	1.3	0.3	HII region
G330.927-00.407	15:45:48.5	-54:04:31	0.22	19.6	812	7995	1.16	0.9	0.3	HII region
G330.958-00.273	15:48:53.2	-54:30:26	0.27	20.0	1029	50090	0.91	1.2	0.4	MIR bright
G331.132-00.245	15:49:56.4	-54:38:26	0.25	31.3	2328	201288	2.56	2.0	0.5	HII region
G331.133-00.525	15:49:03.5	-54:23:38	0.26	23.5	578	37152	0.56	1.3	0.9	ext. HII reg.
G331.230-00.226	15:49:07.8	-54:23:04	0.41	13.2	907	2479	0.36	1.1	0.6	MIR dark
G331.273-00.375	15:49:06.9	-54:21:53	0.41	11.2	2561	1568	1.00	1.0	0.2	starless
G331.340+00.019	15:47:32.7	-53:52:38	0.15	18.4	120	13810	0.35	0.7	0.8	MIR bright
G331.342-00.346	15:51:29.3	-54:31:27	0.30	22.9	986	24380	0.75	0.9	0.3	YSO
G331.434-00.284	15:52:34.4	-54:36:19	0.23	19.4	296	7997	0.37	1.0	0.9	MIR dark
G331.505-00.343	15:52:49.7	-54:36:19	0.15	18.0	176	8049	0.54	0.7	0.4	MIR bright
G331.512-00.103	15:53:00.9	-54:37:34	0.38	27.2	2938	261659	1.33	1.6	0.4	YSO
G331.531-00.101	15:50:18.7	-53:57:03	0.35	17.1	3595	4855	1.90	1.8	0.4	MIR bright
G331.570-00.229	15:49:19.6	-53:45:12	0.19	12.6	453	737	0.86	0.9	0.4	MIR bright
G331.625+00.527	15:54:33.0	-54:12:35	0.19	18.1	459	2836	0.82	1.2	0.7	MIR bright
G331.638+00.501	15:54:38.0	-54:11:23	0.31	9.0	3098	120	2.14	0.8	0.1	starless
G331.693-00.216	15:56:15.8	-54:19:58	0.28	16.1	463	920	0.40	1.2	0.9	MIR bright
G331.708+00.583	15:53:09.6	-53:40:25	0.50	27.8	2856	6588	0.76	1.9	0.7	MIR bright
G331.723-00.203	15:54:34.6	-53:50:41	0.15	17.1	282	7124	0.81	1.4	1.2	MIR bright
G331.857-00.125	15:56:57.7	-53:57:46	0.21	14.3	850	7133	1.24	1.1	0.3	MIR dark
G331.884+00.061	15:52:42.6	-53:09:47	0.29	15.3	1605	9743	1.23	1.6	0.5	MIR bright
G332.094-00.421	15:57:28.5	-53:52:24	0.18	27.2	874	39754	1.77	1.2	0.3	YSO
G332.240-00.043	15:54:06.5	-53:11:38	0.17	19.2	435	3139	1.06	1.3	0.8	MIR bright
G332.278-00.546	15:57:28.3	-52:52:38	0.16	13.7	485	653	1.26	1.0	0.4	MIR bright
G332.294-00.094	15:56:51.3	-52:40:19	0.17	22.4	925	16856	2.08	1.0	0.2	HII region
G332.469-00.523	16:01:10.0	-53:16:00	0.20	19.2	890	89373	1.41	1.3	0.4	YSO
G332.543-00.124	16:01:47.1	-53:11:41	0.22	18.8	712	2525	0.96	0.7	0.2	HII region
G332.558-00.592	16:03:32.4	-53:09:26	0.20	14.3	416	1381	0.70	1.4	1.1	MIR bright
G332.604-00.168	16:02:20.2	-52:55:18	0.15	19.6	169	1535	0.52	1.3	1.6	MIR bright
G332.681-00.008	15:59:36.7	-52:22:53	0.26	9.7	1243	117	1.20	0.7	0.1	starless
G332.695-00.613	15:59:40.7	-52:23:27	0.17	34.7	345	22181	0.84	1.3	0.9	MIR bright
G332.826-00.549	16:01:45.2	-52:40:13	0.32	21.2	5561	424112	3.60	2.1	0.3	HII region

Table B2. Table B1 continues

Clump	RA (°)	Dec (°)	Radius (pc)	Temperature (K)	Mass (M_{\odot})	Luminosity (L_{\odot})	Σ (g cm^{-2})	σ km s^{-1}	α_{vir}	evol. phase
G332.959+00.775	16:00:08.2	-51:37:04	0.17	23.1	183	38152	0.41	1.3	1.9	HII region
G333.029-00.062	16:03:43.6	-51:51:45	0.14	27.0	172	122708	0.60	1.5	2.2	HII region
G333.052+00.030	16:09:22.6	-52:14:48	0.23	23.7	272	115420	0.33	0.8	0.7	ext. HII reg.
G333.130-00.563	16:09:31.3	-52:15:52	0.21	21.0	2145	7452	3.32	1.6	0.3	MIR bright
G333.182-00.396	16:10:40.6	-52:14:37	0.44	15.5	1799	9652	0.62	1.0	0.3	starless
G333.185-00.092	16:10:23.1	-52:06:59	0.20	21.1	413	59749	0.72	1.2	0.8	MIR bright
G333.202-00.045	16:10:44.7	-52:05:50	0.20	14.0	477	9106	0.80	1.0	0.5	MIR bright
G333.203+00.295	16:10:17.9	-51:58:41	0.16	15.5	164	762	0.43	0.9	0.9	MIR bright
G333.234-00.062	16:10:59.8	-51:50:23	0.23	40.0	593	15015	0.79	1.6	1.1	MIR bright
G333.340-00.128	16:09:15.2	-51:32:36	0.34	19.3	1024	5899	0.58	0.9	0.3	HII region
G333.449-00.183	16:12:15.2	-52:02:28	0.26	15.5	128	2745	0.13	1.9	8.0	starless
G333.466-00.165	16:11:21.9	-51:45:30	0.15	27.6	870	17027	2.43	1.4	0.4	ext. HII reg.
G333.480-00.225	16:12:14.6	-51:50:17	0.20	15.8	417	6797	0.69	1.2	0.8	starless
G333.528-00.493	16:10:49.1	-51:30:10	0.26	10.1	1180	110	1.17	0.8	0.2	MIR bright
G333.561-00.023	16:12:26.4	-51:46:13	0.17	16.0	294	523	0.66	1.4	1.3	MIR dark
G333.670-00.352	16:12:35.8	-51:39:42	0.15	15.0	131	1559	0.39	1.4	2.7	starless
G333.755-00.231	16:13:11.8	-51:39:19	0.22	14.0	461	319	0.64	1.2	0.8	MIR bright
G333.759+00.363	16:12:10.6	-51:28:32	0.16	21.2	136	6690	0.36	1.4	2.6	MIR bright
G333.774-00.258	16:12:15.0	-51:27:35	0.19	15.0	374	530	0.69	1.4	1.1	MIR bright
G334.026-00.048	16:12:59.9	-51:31:40	0.29	13.7	1388	37586	1.10	1.3	0.4	HII region
G334.344+00.049	16:09:57.3	-50:56:20	0.82	22.2	4023	58523	0.39	1.5	0.5	ext. HII reg.
G334.656-00.286	16:10:07.9	-50:56:54	0.17	24.0	128	65924	0.31	0.7	0.8	MIR bright
G334.746+00.505	16:13:30.9	-51:26:07	0.18	17.3	311	659	0.62	1.2	1.0	MIR bright
G335.221-00.345	16:10:06.3	-50:50:24	0.15	19.3	227	2210	0.64	1.1	1.0	MIR bright
G335.284-00.134	16:10:01.6	-50:49:29	0.15	16.4	319	9853	0.92	1.2	0.8	MIR bright
G335.349+00.413	16:13:36.2	-51:24:19	0.25	13.2	338	1445	0.37	0.8	0.6	MIR bright
G335.427-00.239	16:13:51.8	-51:15:21	0.16	22.1	302	3876	0.81	1.5	1.3	MIR bright
G335.591+00.184	16:13:11.3	-51:05:52	0.18	10.3	467	624	0.93	1.0	0.4	starless
G335.688-00.813	16:16:16.7	-51:18:22	0.31	17.0	1587	5194	1.11	1.0	0.2	MIR bright
G335.790+00.174	16:15:17.2	-50:55:58	0.16	27.9	951	194865	2.38	1.5	0.4	MIR bright
G337.134+00.007	16:17:41.7	-51:16:02	0.59	14.8	5823	1619	1.13	1.5	0.2	MIR bright
G337.174-00.059	16:15:45.4	-50:55:52	0.60	11.8	11423	53948	2.14	1.1	0.1	ext. HII reg.
G337.705-00.054	16:16:42.9	-50:50:14	0.63	29.2	17125	201807	2.91	2.3	0.2	ext. HII reg.
G337.845-00.376	16:18:26.6	-51:07:08	0.14	40.0	96	434742	0.35	0.9	1.4	HII region
G337.933-00.506	16:17:01.5	-50:46:47	0.40	17.2	3415	26465	1.45	1.0	0.1	MIR dark
G337.973-00.519	16:19:09.6	-51:06:17	0.26	12.5	220	3181	0.22	0.9	1.2	MIR dark
G337.995+00.077	16:17:29.5	-50:46:10	0.48	23.6	2705	222684	0.77	1.4	0.4	HII region
G338.066-00.070	16:17:08.5	-50:36:08	0.21	14.3	599	3048	0.89	1.2	0.6	ext. HII reg.
G338.281+00.541	16:19:52.0	-51:01:29	0.23	18.6	847	8074	1.02	1.3	0.6	YSO
G338.325+00.154	16:20:12.5	-50:53:09	0.12	22.5	114	79901	0.50	1.3	2.0	HII region
G338.423-00.410	16:14:59.8	-49:50:39	0.14	16.4	115	6746	0.39	0.9	1.2	MIR bright
G338.461-00.244	16:21:22.7	-50:52:54	0.21	25.1	511	12294	0.75	0.5	0.1	MIR bright
G338.867-00.479	16:18:56.8	-50:23:50	0.15	9.9	337	48	0.97	1.2	0.8	MIR bright
G338.917+00.382	16:18:39.4	-50:18:55	0.01	23.2	1	13928	0.96	1.3	12.8	HII region
G338.927+00.632	16:20:47.8	-50:38:42	0.27	19.3	2765	11858	2.60	1.7	0.3	MIR bright
G338.935-00.062	16:21:35.8	-50:40:50	0.15	24.7	176	8420	0.49	1.4	2.0	YSO
G339.105+00.148	16:21:06.5	-50:31:43	0.27	23.8	709	163227	0.63	1.4	0.8	HII region
G339.284+00.134	16:19:46.0	-50:18:32	0.22	20.1	515	1311	0.69	1.5	1.2	MIR bright
G339.398-00.415	16:19:38.7	-50:15:50	0.23	14.6	328	577	0.41	1.0	0.8	YSO
G339.476+00.185	16:18:09.7	-50:01:17	0.53	26.0	4147	80996	0.97	1.8	0.5	ext. HII reg.
G339.622-00.122	16:21:18.2	-50:30:15	0.17	24.1	407	13979	0.98	1.1	0.6	YSO
G339.834+00.633	16:19:51.2	-50:15:10	0.23	11.2	660	1880	0.87	0.4	0.1	MIR bright
G339.924-00.084	16:21:42.5	-50:28:06	0.31	18.6	1859	58883	1.26	1.3	0.3	YSO
G340.055-00.244	16:19:28.9	-50:04:41	0.14	23.8	875	36319	2.89	1.6	0.5	HII region
G340.273-00.212	16:20:36.9	-50:13:35	0.24	33.4	1182	7577	1.37	1.2	0.4	ext. HII reg.
G340.307-00.377	16:20:07.7	-50:04:46	0.23	12.6	1010	400	1.22	1.1	0.3	MIR dark
G340.311-00.436	16:21:20.6	-50:11:18	0.50	10.5	4239	2616	1.11	1.0	0.1	MIR bright
G340.401-00.378	16:21:20.2	-50:09:47	0.51	11.7	4758	1680	1.21	1.3	0.2	MIR bright
G340.431-00.372	16:21:40.1	-50:11:45	0.17	17.0	258	1284	0.56	1.1	1.0	YSO
G340.785-00.097	16:23:04.1	-50:20:58	0.47	33.4	2442	161404	0.73	1.3	0.4	MIR bright
G340.878-00.374	16:22:22.7	-50:11:51	0.19	21.4	974	125591	1.83	1.6	0.6	HII region
G341.215-00.236	16:21:08.6	-49:59:44	0.23	21.2	655	92934	0.83	1.1	0.5	HII region

Table B3. Table B1 continues

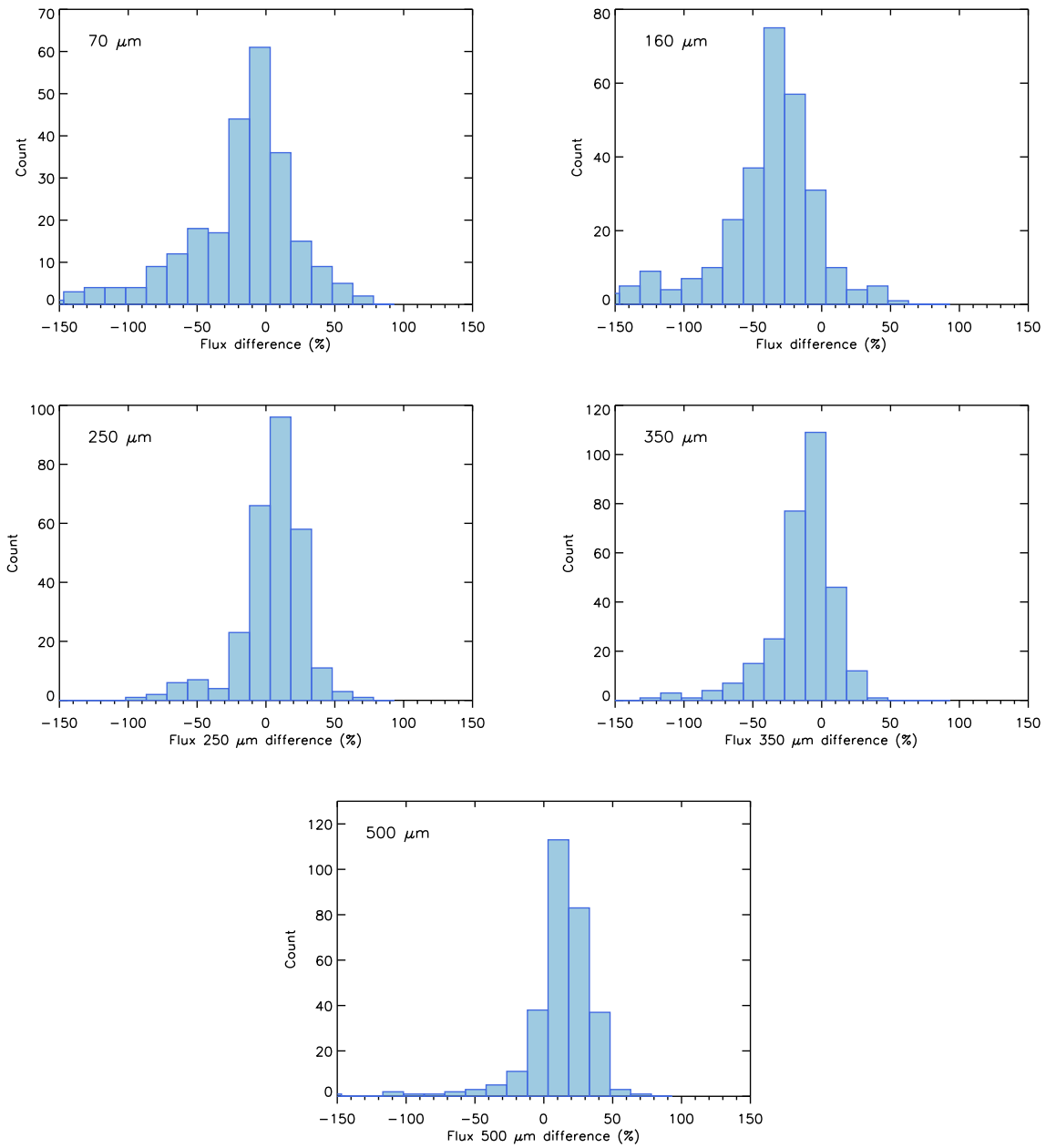
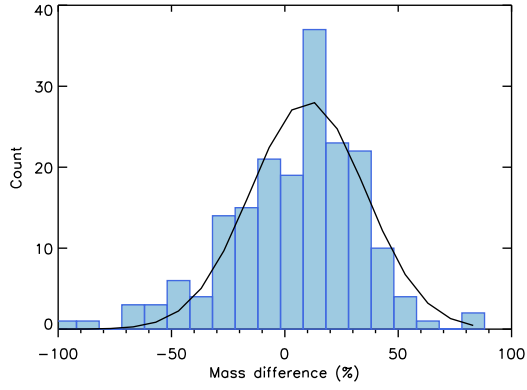


Figure A1. Difference in percentage between the fluxes of the clumps as estimated in Elia et al. (2017) and estimated using the *Hyper* algorithm. *From the top:* Flux difference at 70, 160, 250, 350 and 500 μm respectively.

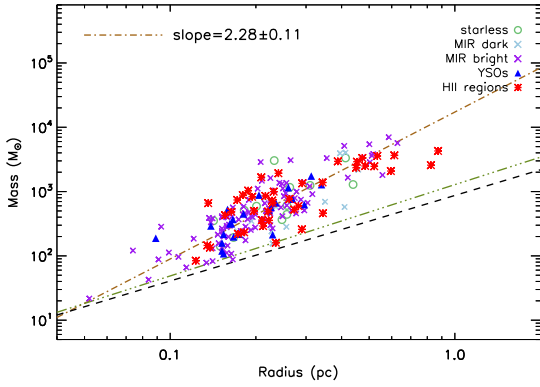
Clump	RA (°)	Dec (°)	Radius (pc)	Temperature (K)	Mass (M_{\odot})	Luminosity (L_{\odot})	Σ (g cm^{-2})	σ km s^{-1}	α_{vir}	evol. phase
G341.218-00.213	16:23:02.8	-50:08:55	0.16	32.2	365	18395	0.96	1.4	1.0	YSO
G341.282-00.295	16:22:53.9	-50:00:21	0.26	15.2	848	5444	0.85	1.4	0.7	MIR bright
G342.369+00.140	16:20:19.1	-49:34:51	0.05	19.4	27	22213	0.68	1.3	3.5	MIR bright
G342.415+00.412	16:23:06.0	-50:00:36	0.56	14.2	3398	10881	0.73	0.6	0.1	MIR bright
G342.484+00.183	16:23:17.2	-49:40:59	0.63	22.2	6698	19631	1.12	1.1	0.1	MIR bright
G342.706+00.125	16:21:37.1	-49:23:28	0.04	28.8	30	52852	1.60	1.6	3.4	HII region
G342.822+00.382	16:24:14.2	-49:23:25	0.42	13.5	1594	2519	0.60	1.2	0.4	MIR bright
G342.959-00.318	16:27:02.6	-49:24:00	0.17	20.6	213	44215	0.51	1.2	1.2	YSO
G343.134-00.484	16:23:58.3	-48:46:58	0.22	13.6	321	128	0.45	1.4	1.5	MIR bright
G343.501+00.025	16:27:26.2	-49:12:34	0.03	14.8	14	13364	1.41	1.1	2.6	MIR bright
G343.503-00.015	16:29:41.5	-49:01:58	0.18	23.2	719	461495	1.47	1.3	0.5	HII region
G343.520-00.519	16:29:01.3	-48:50:27	0.16	21.3	348	3066	0.86	1.2	0.9	YSO
G343.689-00.018	16:26:55.0	-48:24:58	0.16	20.0	275	1224	0.71	1.0	0.6	MIR bright
G343.720-00.223	16:30:05.7	-48:48:42	0.16	21.3	295	3602	0.75	0.9	0.5	MIR bright
G343.737-00.113	16:30:57.9	-48:43:45	0.14	14.6	343	436	1.15	1.2	0.7	MIR bright
G343.756-00.163	16:28:55.0	-48:24:01	0.15	23.8	680	14171	2.12	1.2	0.4	MIR bright
G343.938+00.097	16:33:43.6	-49:00:47	0.11	14.9	51	444	0.27	1.0	2.6	MIR bright
G344.101-00.661	16:29:47.1	-48:15:49	0.14	21.5	281	6584	0.97	1.6	1.6	MIR bright
G344.221-00.594	16:35:06.2	-48:46:14	0.16	34.1	336	37800	0.92	1.3	1.0	HII region
G344.246-00.670	16:33:29.5	-48:03:43	0.05	10.6	24	91	0.58	1.3	4.0	starless
G344.726-00.541	16:34:13.2	-48:06:15	0.14	10.2	292	50	0.95	0.9	0.5	starless
G345.132-00.175	16:34:11.1	-47:33:24	0.09	18.4	98	747	0.80	1.1	1.3	MIR bright
G345.144-00.217	16:34:38.7	-47:36:28	0.11	16.8	107	896	0.62	1.0	1.1	MIR bright
G345.718+00.818	16:33:40.1	-47:23:28	0.09	18.5	207	1069	1.75	1.1	0.7	YSO
G346.078-00.056	16:36:17.2	-47:40:46	0.60	21.8	4806	83689	0.89	1.5	0.3	HII region
G347.967-00.434	16:35:58.7	-47:23:36	0.41	18.9	4779	118251	1.86	1.5	0.2	MIR dark
G348.171+00.465	16:36:18.9	-47:23:17	0.07	16.7	168	390	2.03	1.1	0.6	MIR bright
G348.181+00.482	16:36:25.5	-47:24:26	0.08	22.1	337	1448	3.41	1.0	0.3	MIR bright
G349.092+00.106	16:36:15.4	-47:19:02	0.47	40.0	1277	142104	0.38	1.7	1.2	MIR bright

Table B4. Table B1 continues



!th

Figure A2. Mass differences (*Cutex* - *Hyper* values) for the 192 clumps with properties measured as in the Elia et al. (2017) catalogue and using *Hyper*. The black curve is the Gaussian fits to the distribution, used to estimate the uncertainties associated with the dust photometry.



!th

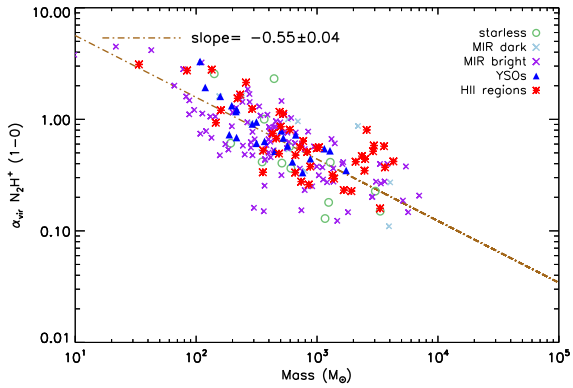


Figure A3. From the top: same of Figures 8 and 9 but assuming the dust parameters estimated using *Hyper*. The slopes of the diagrams are consistent with the findings discussed in the paper.

